

Quarterly Technical Report

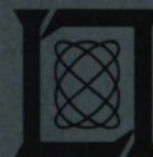
Solid State Research

1987:4

Lincoln Laboratory

MASSACHUSETTS INSTITUTE OF TECHNOLOGY

LEXINGTON, MASSACHUSETTS



Prepared under Electronic Systems Division Contract F19628-85-C-0002.

Approved for public release; distribution unlimited.

ADA194708

The work reported in this document was performed at Lincoln Laboratory, a center for research operated by Massachusetts Institute of Technology, with the support of the Department of the Air Force under Contract F19628-85-C-0002.

This report may be reproduced to satisfy needs of U.S. Government agencies.

The views and conclusions contained in this document are those of the contractor and should not be interpreted as necessarily representing the official policies, either expressed or implied, of the United States Government.

The ESD Public Affairs Office has reviewed this report, and it is releasable to the National Technical Information Service, where it will be available to the general public, including foreign nationals.

This technical report has been reviewed and is approved for publication.

FOR THE COMMANDER

Hugh L. Southall

Hugh L. Southall, Lt. Col., USAF
Chief, ESD Lincoln Laboratory Project Office

Non-Lincoln Recipients

PLEASE DO NOT RETURN

Permission is given to destroy this document
when it is no longer needed.

**MASSACHUSETTS INSTITUTE OF TECHNOLOGY
LINCOLN LABORATORY**

SOLID STATE RESEARCH

QUARTERLY TECHNICAL REPORT

1 AUGUST — 31 OCTOBER 1987

ISSUED 11 MARCH 1988

Approved for public release; distribution unlimited.

LEXINGTON

MASSACHUSETTS

ABSTRACT

This report covers in detail the solid state research work of the Solid State Division at Lincoln Laboratory for the period 1 August through 31 October 1987. The topics covered are Solid State Device Research, Quantum Electronics, Materials Research, Microelectronics, and Analog Device Technology. Funding is provided primarily by the Air Force, with additional support provided by the Army, DARPA, Navy, SDIO, NASA, and DOE.

TABLE OF CONTENTS

Abstract	iii
List of Illustrations	vii
List of Tables	xi
Introduction	xiii
Reports on Solid State Research	xvii
Organization	xxv
 1. SOLID STATE DEVICE RESEARCH	 1
1.1 Monolithic Two-Dimensional Surface-Emitting Arrays of GaAs/AlGaAs Diode Lasers	1
1.2 Integrated Optics Wavefront Measurement Sensor	4
1.3 Stabilization of the Optical Power of a Laser Diode	8
 2. QUANTUM ELECTRONICS	 13
2.1 Synchronously Pumped Mode-Locked Ti:Al ₂ O ₃ Laser	13
2.2 Tuning Experiments on a Ti:Al ₂ O ₃ Laser Using an Interferometric Cavity	13
2.3 Small-Signal Gain Measurements in a Ti:Al ₂ O ₃ Amplifier	16
2.4 Lidar Observation of the Earth's Sodium Layer	19
 3. MATERIALS RESEARCH	 23
3.1 Residual Infrared Absorption in Ti:Al ₂ O ₃ Crystals	23
3.2 Pt-Ir Silicide Schottky-Barrier IR Detectors	24
 4. MICROELECTRONICS	 31
4.1 New MBE Buffer for Micron- and Quarter-Micron-Gate GaAs MESFETs	31
4.2 Advanced Device Fabrication with Angled Chlorine Ion-Beam-Assisted Etching	35
4.3 Switched-Capacitor Filters	41
 5. ANALOG DEVICE TECHNOLOGY	 45
5.1 RF Surface Resistance of YBa ₂ Cu ₃ O _{7-x} Thin Films	45
5.2 Laser Direct Write Compensation of Reflective-Array Compressor	49
5.3 Bulk-Acoustic-Wave Reflection-Grating Resonators: Phase-Noise Measurements and Temperature Compensation	51

LIST OF ILLUSTRATIONS

Figure No.		Page
1-1	Schematic Diagram of a Monolithic Two-Dimensional Surface-Emitting GaAs/AlGaAs Diode Laser Array with Light Emission from Both Laser Facets of Each Laser. Arrays with Light Emission from Only One Facet of Each Laser Also Were Fabricated	2
1-2	Near-Field Pattern of a 22-Element Array with Light Emission from Both Facets of Each Laser	3
1-3	Pulsed Power Output vs Current of Two-Dimensional Array Whose Near-Field Pattern Is Shown in Figure 1-2. The Current Pulses Were 100 ns Wide at a 1-kHz Repetition Rate	3
1-4	Near-Field Pattern of a 96-Element Array with Light Emission from Only One Facet of Each Laser	4
1-5	The Experimental Arrangement for High-Temporal-Resolution Measurements at $\lambda = 0.514 \mu\text{m}$ in Which the Wavefront Is Tilted by Means of an Acousto-optic Cell	5
1-6	Tilt Measurement Errors for Ten 200-ns-Duration Measurements Taken as the Acousto-optic Cell Tilts the Wavefront at the IOWMS by 2.5 mrad (Corresponding to 45° of Phase) in $2 \mu\text{s}$. These Errors Are Due in Large Part to the Statistics Associated with the Limited Number of Electrons in the CCD Imager Charge Packets	7
1-7	Block Diagram of the Experimental Setup for Controlling the Optical Power from a Semiconductor Laser Diode at Operating Points both Above and Below the Laser Threshold	9
1-8	Performance of Implementation Shown in Figure 1-7. The Difference Between the Measured and Calculated Optical Power Levels, Normalized by the Power in the Least Significant Bit (LSB) Is Plotted vs the Bit Number, Activated Individually. Data Were Taken with the Most Significant Bit (MSB) Off and On	10
2-1	Laser Cavity Geometry. B.S. Is a Beamsplitter, Coated on One Side with a 3% Reflecting Thin Film; the Opposite Side Is Used at Brewster's Angle	14
2-2	Combined Mechanical-Electro-optic Tuning. D Is a Position-Sensing Silicon Photodiode	15

Figure No.		Page
2-3	Wavelength Transient Response to a Square-Wave Drive Applied to the Tuning Mirror. Upper Trace: Open Loop Response. Lower Trace: with Feedback from Wavelength-Sensing Detector (Figure 2-2).	15
2-4	Schematic of the Experimental Setup for the Measurement of Small-Signal Double-Pass Gain in a $\text{Ti:Al}_2\text{O}_3$ Amplifier. A Frequency-Doubled Nd:YAG Laser Served as the Pump Source and Either a CW He-Ne Laser or a CW $\text{Ti:Al}_2\text{O}_3$ Was Used as the Signal Source. Single-Pass Measurements Were Made Along the Indicated Path with the Tuning Mirrors Removed and the Detector Repositioned	16
2-5	The Exponential Gain g_0L as a Function of Incident Pump Energy Density for the Single- and Double-Pass Experiments at 790.7 nm and 799.8 nm, Respectively, with a $\text{Ti:Al}_2\text{O}_3$ Laser Used as the Signal Source. The Lines Through the Data Are Linear Fits with the Constraint That They Pass Through the Origin	17
2-6	The Gain Anisotropy Between the π and σ Polarizations at 632.8 nm. The Angle Between the Polarization Vector of the He-Ne Laser and the c-Axis Is θ . The Straight Line Is a Linear Fit of the Data to the Equation $g_o = g_\pi - (g_\pi - g_\sigma)\sin^2\theta$. The Incident Pump Energy Density Was 3.7 J/cm^2	18
2-7	The Observed Pulse Width $t_{1/e}$ at 790.7 nm as a Function of Incident Pump Energy Density. The Time Required for the Signal Intensity to Reach $1/e$ of Its Value at $t = 0$ Is Defined as $t_{1/e}$. The Data Are Indicated by the Circles, While the Solid Line Is Given by Equation (2-2)	19
2-8	Schematic of the Sodium-Fluorescence-Detection Apparatus	20
2-9	Sodium-Resonance Radiation Backscattered by the Earth's Atmosphere. Photomultiplier Counts per Microsecond Over 2×10^6 Laser Pulses Are Plotted as a Function of the Elapsed Time After the Sodium-Resonance-Radiation Pulse Is Transmitted into the Atmosphere. The Signal from the Sodium Layer Occurs at a Round-Trip Time of $600 \mu\text{s}$	21
3-1	Residual Absorption Coefficient α_r at 780 nm vs Main Absorption Coefficient α_m at 490 nm Measured at Room Temperature in the π Polarization for a Partially Oxidized VGF Sample of $\text{Ti:Al}_2\text{O}_3$	25

Figure No.		Page
3-2	Plot of α_r/α_m vs α_m Obtained from Data of Figure 3-1. Values of C and α_0 Determined from the Straight Line in Accordance with Equation (3-2) Were Used to Calculate the Parabola Shown in Figure 3-1	25
3-3	Schematic Structure of Silicide Schottky-Barrier Infrared Detector with Pt-Ir Silicide Electrode	26
3-4	(a) Forward and (b) Reverse Current-Voltage Characteristics at 77 K for Pt, Ir, and Pt-Ir Silicide Schottky-Barrier Diodes	27
3-5	Responsivity as a Function of Wavelength for Pt, Ir, and Pt-Ir Silicide Schottky-Barrier Detectors	28
4-1	Schematic Cross Section of the MESFET Structure Used to Measure Backgating	31
4-2	Backgating Characteristics: New MBE Buffer, Undoped GaAs Buffer, and Undoped Superlattice Buffer. The Solid Lines Indicate the Results Obtained in the Dark, and the Dashed Lines in the Light	32
4-3	SEM Photographs of the 0.27- μ m MESFET: (a) Top View of the Device, and (b) Magnified View of the Gate Region	33
4-4	Schematic Cross Sections of the 0.27- μ m MESFETs: (a) New MBE Buffer, and (b) Undoped GaAs Buffer	34
4-5	(a) Schematic Diagram of a Monolithic Surface-Emitting Two-Dimensional GaAs/AlGaAs Laser Diode Array, and (b) Near-Field Pattern of a Typical Array	36
4-6	Schematic Diagram Illustrating the Two-Step Process for Fabricating Nanometer-Size Structures Such as Quantum Wires. After the Initial Etch, the Masking Layer Is Removed and a Second Angled Etch Is Used to Thin the Columns	37
4-7	SEM Micrographs Showing (a) 80-nm-Wide Columns Resulting from a Normal-Incident Chlorine IBAE Etch, and (b), (c), and (d) the Results of Angle Etching the 80-nm-Wide Columns of Micrograph (a). The Columns in Micrographs (b), (c), and (d) Were Etched for 1.0, 1.5, and 2.0 min, Respectively, and Have Respective Widths of 40, 22, and 9 nm	38

Figure No.		Page
4-8	Schematic Diagram Showing a Scheme for Contacting the Quantum Well of a Resonant Tunneling Transistor. The Key Fabrication Steps Include an Angle Etch, MBE Overgrowth, Top Contact Shadow Evaporation, Reactive Ion Etching or Second Chlorine IBAE to Open the Well Contact, and Well Contact Evaporation	39
4-9	Schematic Diagram of the Proposed Resonant Tunneling Transistor with SEM Micrographs Showing the Finger Structure After Angled Chlorine IBAE. As Shown in the Micrographs, a Compound Angle Cut Was Used Also to Aid in Contact Isolation	40
4-10	Schematic Diagram of the Proposed Vertical FET. In This Device, the Pinch-Off Voltage Is Adjusted with Angled Etching Before the Gates Are Applied	40
4-11	Switched-Capacitor Lowpass Filter. (a) Conceptual Representation. (b) Realization with MOSFET Transfer Gates Controlled by Nonoverlapping Clocks	41
4-12	Step Response of the Switched-Capacitor Filter at a Clock Frequency of 1 MHz. (a) Measured Response at an Update Rate of 15 μ s. (b) Calculated Response at an Update Rate of 30 μ s	42
5-1	Cross Section of the Stripline Resonator	46
5-2	Meander-Line Pattern Used for the Center Conductor of the Resonator	46
5-3	Surface Resistance of YBaCuO, Au, and Al Films as a Function of Frequency at 4.2K	48
5-4	Measured Values of the Dielectric Loss Tangent of Yttria-Stabilized Zirconia Substrates at T = 4.2 K	49
5-5	RAC Frequency Response Before and After Full Compensation. Vertical Lines Near Upper Frequency Axis Indicate the Design Bandwidth of This Device	50
5-6	Corresponding RAC Phase Errors. A Single Phase-Compensation Pattern Was Applied After Amplitude Correction	51

Figure No.		Page
5-7	Results of Measurements of Phase Noise in BAW-Resonator-Stabilized Oscillators. For Reference, the Noise in a Typical SAW Oscillator Multiplied up to 1-GHz Operation and Noise for a DRO at 1 GHz Are Shown. Also Shown Is a Theoretical Curve Obtained Using Equation (5-6) with $G = 40$ dB, $F = 3$ dB, $P_c = 16$ dBm, $Q = 2.0 \times 10^4$, and $\alpha = 1.6 \times 10^{-11}$. The Agreement Between Theory and Experiment Is Excellent. The Bottom Curve Shows the Projected Noise with Improvements Discussed in Text, Using Equation (5-6) with $G = 25$ dB, $F = 4$ dB, $P_c = 27$ dBm, $Q = 5 \times 10^4$, and $\alpha = 2 \times 10^{-12}$	52
5-8	Reflection Coefficient for a Resonator Fabricated in LiTaO ₃	53
5-9	Measurements of Relative Change in Delay vs Temperature for New Cut of LiTaO ₃ Employing Shear Wave Propagation	54

LIST OF TABLES

Table No.		Page
4-1	Summary of RF Results	34
5-1	Thin Film Parameters	45

INTRODUCTION

1. SOLID STATE DEVICE RESEARCH

Monolithic two-dimensional GaAs/AlGaAs diode laser arrays with light emission normal to the surface have been fabricated using edge-emitting quantum-well lasers with facets and adjacent deflecting mirrors formed by ion-beam-assisted etching. A pulsed output power density of 370 W/cm^2 was obtained from a 22-element array, and a total output power of 7 W (limited by available current) was obtained from a 96-element array.

The integrated optics wavefront measurement sensor has been used to measure a wavefront deflected at high speed by an acousto-optic cell. Ten 200-ns-duration frames of data have been obtained, and the phase angle of the optical wavefront has been measured with an rms error of 3° .

Design considerations have been formulated for an optical power controller that is capable of stabilizing a laser diode output at operating points both above and below the laser threshold current. An 8-bit experimental implementation has yielded results in good agreement with expectations.

2. QUANTUM ELECTRONICS

Mode-locked laser operation has been obtained in a $\text{Ti:Al}_2\text{O}_3$ ring laser synchronously pumped by a frequency-doubled Nd:YAG laser-amplifier system. This is the first time mode-locked lasing has been achieved by synchronous pumping in either a solid-state material or in a system with a lifetime greater than $1 \mu\text{s}$.

A laser cavity with a weakly coupled side arm has been used successfully for wideband tuning of the $\text{Ti:Al}_2\text{O}_3$ master oscillator, providing tolerance of high intra-cavity insertion losses and operation at low optical intensity. In a mixed mechanical-electro-optic approach to the frequency agility requirements, coarse tuning over most of the $\text{Ti:Al}_2\text{O}_3$ laser gain curve has been achieved in less than 1 ms.

A small-signal, single-pass power gain of 180 has been measured for an input signal in the polarization parallel to the c-axis at 790.7 nm in a longitudinally pumped $\text{Ti:Al}_2\text{O}_3$ amplifier, and a double-pass power gain of 10^4 has been obtained for the same polarization at 799.8 nm. The lifetime of the upper laser level decreases with increased pumping, probably as a result of amplified spontaneous emission.

Resonance fluorescence from the earth's naturally occurring sodium layer, at 90 km altitude, has been observed using a solid-state source of pulsed sodium-resonance radiation generated by sum-frequency mixing the output of two pulsed Nd:YAG lasers. The number of backscattered photons was counted as a function of time after the pulse of sodium-resonance radiation was transmitted vertically into the atmosphere.

3. MATERIALS RESEARCH

Measurements have been made on a partially oxidized sample of $\text{Ti:Al}_2\text{O}_3$, in which the $\text{Ti}^{3+}/\text{Ti}^{4+}$ ratio varies with distance from the surface, to determine the residual infrared absorption as a function of the Ti^{3+} absorption for constant total Ti concentration. The results confirm that the residual absorption, which impairs the performance of $\text{Ti:Al}_2\text{O}_3$ tunable lasers, is due to $\text{Ti}^{3+}\text{-Ti}^{4+}$ pairs.

Schottky-barrier infrared detectors have been fabricated with silicide electrodes formed by sequential vacuum deposition of 5 to 10 Å thick Pt and 10 to 20 Å thick Ir layers on p-type Si substrates and subsequent thermal annealing. The Pt-Ir silicide diodes have cutoff wavelengths extending well beyond 6 μm and exhibit higher quantum efficiency than either Pt-only or Ir-only silicide diodes over a significant spectral range.

4. MICROELECTRONICS

A new buffer layer has been developed that eliminates backgating in GaAs MESFETs and substantially reduces short-channel effects in GaAs MESFETs with 0.27-μm-long gates. The new buffer layer, which is crystalline, highly resistive, optically inactive, and can be overgrown with high quality GaAs, is grown by molecular beam epitaxy at a substrate temperature of 200°C using Ga and As_4 beam fluxes.

Angled ion-beam-assisted etching has been used in conjunction with a variety of lithographic techniques to produce structures in GaAs and GaAlAs with controlled side-wall geometries. Vertical field effect transistors, resonant tunneling transistors, surface emitting laser arrays and quantum-wire structures have been fabricated.

A switched-capacitor low-pass filter has been integrated into each of 700 fingers of an enhanced design of the SAW/FET wideband tapped delay line. The new SAW/FET shows improved performance, and switched-capacitor-filter test structures on the same chips perform in agreement with SPICE simulations used in the design.

5. ANALOG DEVICE TECHNOLOGY

The surface resistance of superconducting polycrystalline thin films of $\text{YBa}_2\text{Cu}_3\text{O}_{7-x}$ has been measured in the frequency range between 0.5 GHz and 17 GHz at low temperatures using a stripline-resonator method. The value of the surface resistance at 4.2 K and 1 GHz is $7 \times 10^{-4} \Omega$, less than that of any normal metal, and is proportional to the square of the frequency, as is that of conventional superconductors.

Laser-activated photochemical techniques have been used to define amplitude- and phase-correction patterns of $\text{Cr-Cr}_2\text{O}_3$ and Mo, respectively, contained between reflective-array-compressor gratings. With the incorporation of a recently developed compensation algorithm, which includes the coupling between amplitude and phase, amplitude compensation to within ± 0.05 dB of the desired uniform response and rms residual phase error of 0.5° have been achieved over the design bandwidth.

The phase noise of lithium niobate holographic bulk-acoustic-wave reflection-grating oscillators operating at 1 GHz has been measured to be -150 dBc/Hz at 100-kHz offset from the carrier. Measurements of holographic gratings in iron-doped lithium tantalate indicate that high-quality-factor resonators can be fabricated in this temperature-compensated material.

REPORTS ON SOLID STATE RESEARCH

1 August through 31 October 1987

PUBLISHED REPORTS

Journal Articles

JA No.

5933	Analysis of Junction Depths and Lattice Point Defect Interdiffusion Coefficients in $\text{Hg}_{0.8}\text{Cd}_{0.2}\text{Te}$	T.C. Harman	J. Vac. Sci. Technol. A 5 , 3055 (1987)
5967	High-Temperature Point-Contact Transistors and Schottky Diodes Formed on Synthetic Boron-Doped Diamond	M.W. Geis D.D. Rathman D.J. Ehrlich R.A. Murphy W.T. Lindley	IEEE Electron Device Lett. EDL-8 , 341 (1987)
5968	Zone-Melting-Recrystallization Silicon-on-Insulator Technology	B-Y. Tsaur	IEEE Circuits Devices Mag. 3 , 12 (1987)
5972	Acousto-optic Modulator as an Electronically Selectable Unidirectional Device in a Ring Laser	R. Roy* P.A. Schultz A. Walther	Opt. Lett. 12 , 672 (1987).
5979	Multistable Mode Locking of InGaAsP Semiconductor Lasers	M. Kuznetsov* D.Z. Tsang J.N. Walpole Z.L. Liao E.P. Ippen*	Appl. Phys. Lett. 51 , 895 (1987)
5990	Comment on "Observation of Intrinsic Disability in Resonant Tunneling Structures"	T.C.L.G. Sollner	Phys. Rev. Lett. 59 , 1622 (1987)
6007	Microwave MESFET's Fabricated in GaAs Layers Grown on SOS Substrates	G.W. Turner H.K. Choi B-Y. Tsaur	IEEE Electron Device Lett. EDL-8 , 460 (1987)
6009	Monolithic Two-Dimensional Surface-Emitting Arrays of GaAs/AlGaAs Diode Lasers	J.P. Donnelly W.D. Goodhue T.H. Windhorn R.J. Bailey S.A. Lambert*	Appl. Phys. Lett. 51 , 1138 (1987)

* Author not at Lincoln Laboratory.

JA No.

- | | | | |
|------|---|--|--|
| 6021 | Preparation of Superconducting YBa ₂ Cu ₃ O _x Thin Films by Oxygen Annealing of Multilayer Metal Films | B-Y. Tsaur
M.S. DiIorio
A.J. Strauss | Appl. Phys. Lett. 51 , 858 (1987) |
| 6028 | Surface-Emitting Semiconductor Diode Lasers | J.N. Walpole | Laser Focus 23 , 66 (1987) |

Meeting Speeches**MS No.**

- | | | | |
|------|---|---|--|
| 7393 | Picosecond Optoelectronic Switches Using Composite Electronic Materials | E.A. Chauchard*
C.H. Lee*
V. Diadiuk
G.W. Turner | Technical Digest, 2nd Topical Meeting on Picosecond Electronics, Incline Village, Nevada, 12 January 1987, Paper WE12, p. 89 |
| 7426 | Prospects for Monolithic GaAs/Si Integration | H.K. Choi
G.W. Turner
B-Y. Tsaur | Materials Research Society Symposium 91 , 213 (1987) |
| 7444 | Monolithic Two-Dimensional Diode Laser Arrays | J.N. Walpole
Z.L. Liao | <i>Laser Radar II</i> , R.J. Becherer and R.C. Harney, Eds., Proc. SPIE 783 , 42-48 (1987) |

* * * * *

UNPUBLISHED REPORTS**Journal Articles****JA No.**

- | | | | |
|------|---|---|--|
| 6008 | Characterization of Mass-Transported p-Substrate GaInAsP/InP Buried-Heterostructure Lasers with Analytical Solutions for Electrical and Thermal Resistances | Z.L. Liao
J.N. Walpole
D.Z. Tsang
V. Diadiuk | Accepted by IEEE J. Quantum Electron. |
| 6025 | 30-μm Heterodyne Receiver | T. Kostiuk*
D.L. Spears | Accepted by Int. J. Infrared Millimeter Waves |
| 6027 | Monolithic GaAs/Si Optoelectronic Integrated Circuits | H.K. Choi | Accepted by Optoelectronics-Devices and Technologies |

* Author not at Lincoln Laboratory.

JA No.

6029	A Review of Excimer Laser Projection Technology	M. Rothschild D.J. Ehrlich	Accepted by J. Vac. Sci. Technol.
6044	Infrared Anisotropy of $\text{La}_{1.85}\text{Sr}_{0.15}\text{CuO}_{4-y}$	G.L. Doll* J. Steinbeck* G. Dresselhaus* M.S. Dresselhaus* A.J. Strauss H.J. Zeiger	Accepted by Phys. Rev.

Meeting Speeches †

MS No.

6714E	Radiation Damage in Dry Etching	S.W. Pang M.W. Geis	The 1987 Fall Meeting of the Electrochemical Society, Honolulu, Hawaii, 18-23 October 1987
7421A	Microwave and Millimeter-Wave Resonant Tunneling Devices	T.C.L.G. Sollner E.R. Brown W.D. Goodhue	
7567	Laser-Direct-Writing Techniques for Tuning and Modification of Interconnections on Integrated and Multiple-Chip Circuits	J.G. Black C.L. Chen M. Rothschild S.P. Doran L.J. Mahoney D.J. Ehrlich	
7351A	A 100-ns 16-Point Discrete Cosine Transform Processor	A.M. Chiang	SPIE Conference on Visual Communication and Image Processing (II), Cambridge, Massachusetts 25-30 October 1987
7680	A Video-Rate CCD Two-Dimensional Cosine Transform Processor	A.M. Chiang	
7451B	Progress in Tunable $\text{Ti:Al}_2\text{O}_3$ Lasers	A. Sanchez	Seminar on Modern Optics and Spectroscopy, Massachusetts Institute of Technology, Cambridge, Massachusetts, 20 October 1987.

* Author not at Lincoln Laboratory.

† Titles of Meeting Speeches are listed for information only. No copies are available for distribution.

MS No.

7491	Analog Superconductive Correlator for Wideband Signal Processing	J.B. Green A.C. Anderson R.S. Withers	1987 International Superconductivity Conference, Tokyo, Japan, 28-29 August 1987
7491B	Analog Superconductive Correlator for Wideband Signal Processing	J.B. Green A.C. Anderson R.S. Withers	1987 Workshop on Superconducting Electronics, Orange County, California, 26-30 October 1987
7503	Experimental Evaluation of Drift and Nonlinearities in Lithium Niobate Interferometric Modulators	G.E. Betts L.M. Johnson	SPIE's 31st Annual International Technical Symposium on Optical and Optoelectronic Applied Science and Engineering, San Diego, California, 16-21 August 1987
7581	Multiple-Quantum-Well CCD Spatial Light Modulators	B.F. Aull B.E. Burke K.B. Nichols W.D. Goodhue	
7524	Electro-optical Study of $\text{Al}_x\text{Ga}_{1-x}\text{As}/\text{GaAs}$ Coupled Quantum Wells	H.Q. Le J.V. Hryniewicz W.D. Goodhue V.A. Mims	3rd International Conference on Superlattices, Microstructures, and Microdevices, Chicago, Illinois, 17-20 August 1987
7540	A Real Time CCD Parallel Radar Processor	A.M. Chiang	SPIE Symposium on Real Time Signal Processing, San Diego, California, 16-21 August 1987
7553	Advanced Device Fabrication with Angled Chlorine Ion Beam Assisted Etching	W.D. Goodhue S.W. Pang M.A. Hollis	Conference on Advanced Concepts in High Speed Semiconductor Devices and Circuits, Eleventh Biennial Conference, Cornell University/IEEE, Ithaca, New York, 10-12 August 1987
7557	New MBE Buffer for Micron and Quarter-Micron Gate GaAs MESFETs	F.W. Smith A.R. Calawa C.L. Chen L.J. Mahoney M.J. Manfra J.C. Huang* F.H. Spooner*	
7563	Current Directions in Resonant Tunneling Research	T.C.L.G. Sollner	

* Author not at Lincoln Laboratory.

MS No.

7570	High-Power-Added Efficiency Measured at 1.3 and 20 GHz Using a GaAs Permeable Base Transistor	K.B. Nichols M.A. Hollis C.O. Bozler M.A. Quddus L.J. Kushner R. Mathews A. Vera S. Rabe R.A. Murphy D.L. Olsson*	Conference on Advanced Concepts in High Speed Semiconductor Devices and Circuits, Eleventh Biennial Conference, Cornell University/IEEE, Ithaca, New York, 10-12 August 1987
7584	A New Method to Detect Ballistic Electrons in GaAs	W.D. Goodhue E.R. Brown	
7556	On the Applications of Laser-Direct-Writing Techniques to GaAs Monolithic Microwave Integrated Circuits	C.L. Chen J.G. Black W.E. Courtney S.P. Doran L.J. Mahoney M. Rothschild D.J. Ehrlich R.A. Murphy	1987 IEEE GaAs IC Symposium, Portland, Oregon, 13-16 October 1987
7579	Optical Computing	R.C. Williamson	National Communications Forum, Rosemont, Illinois, 29 September-1 October 1987
7582	Phase Noise of Bulk-Acoustic-Wave Reflection-Grating Resonators	D.E. Oates J.Y. Pan	1987 IEEE Ultrasonics Symposium, Denver, Colorado, 14-16 October 1987
7583	MBE-Grown Spatial Light Modulators with Charge-Coupled Addressing	W.D. Goodhue B.E. Burke B.F. Aull K.B. Nichols	8th MBE Workshop, Los Angeles, California, 9-11 September 1987
7587	Laser Direct-Write Compensation of RACs	V.S. Dolat J.H.C. Sedlacek D.J. Ehrlich	1987 IEEE Ultrasonics Symposium, Denver, Colorado, 14-16 October 1987
7591	Acousto-optic Modulator as a Unidirectional Device in a Ring Laser	P.A. Schulz R. Roy*	1987 OSA Annual Meeting, Rochester, New York, 18-23 October 1987

* Author not at Lincoln Laboratory.

MS No.

7593	Near-Field Distribution and Output Wavelength Tuning of a Coherent Array of Discrete Diode Lasers	R.H. Rediker S.K. Liew C. Corcoran	} 1987 OSA Annual Meeting, Rochester, New York, 18-23 October 1987
7595	Direct and Heterodyne Detectors for the Infrared	D.L. Spears	
7601	The Growth of GaAs on Si for Device Applications	G.W. Turner	Symposium on Heteroepitaxy: Principles, Microstructures and Stresses, Cincinnati, Ohio, 12-16 October 1987
7606	Sum Frequency Mixing of Two Tunable Nd:YAG Lasers for Sodium Fluorescence Lidar Measurements	T.H. Jeys	} 1987 Topical Meeting on Laser and Optical Remote Sensing, North Falmouth, Massachusetts, 28 September- 1 October 1987
7607	DIAL Measurements of Atmospheric Water Vapor, HCl, and CH ₄ using a Continuously Tunable 1.7 μ m Co:MgF ₂ Laser	D.K. Killinger N. Menyuk	
7640	Enhanced Direct-Detection of CO ₂ Lidar Returns Using a Laser Pre-amplifier	D.K. Killinger J.L. Bufton* E.J. McLellan*	
7617A	Monolithic GaAs/Si Integration for Optical Interconnects	H.K. Choi	Seminar, Polaroid Corporation, Cambridge, Massachusetts, 14 August 1987
7622	A Comparison of SAW- and CCD-Based Signal Processing	S.C. Munroe D.R. Arsenault R.W. Ralston	1987 IEEE Ultrasonics Symposium, Denver, Colorado, 14-16 October 1987
7634	16-GHz Analog and 16-Gbit/s Digital Modulation of p-Type Substrate Mass-Transported Diode Lasers	D.Z. Tsang Z.L. Liao	MILCOM'87 Washington, D.C., 19-22 October 1987
7645	Superconductive Signal-Processing Devices	R.S. Withers	IEEE Instrumentation and Measurements Society, MIT Magnet Laboratory, Cambridge, Massachusetts, 17 September 1987
7656	Two-Dimensional Arrays of GaInAsP/InP Diode Lasers	J.N. Walpole	IEEE LEOS Seminar, Waltham, Massachusetts, 10 September 1987

* Author not at Lincoln Laboratory.

MS No.

7659	Surface-Emitting GaInAsP/InP Diode Lasers Fabricated by Mass Transport	J.N. Walpole	Compound Semiconductor Growth Processing and Devices: Japan/U.S., Gainesville, Florida, 28 October 1987
7662	Electronic Artificial Neural Networks	J.P. Sage	1987 IEEE Systems, Man and Cybernetics Conference, Alexandria, Virginia, 22 October 1987
7666	Small-Signal Gain Measurements in a Ti:Al ₂ O ₃ Amplifier	K.F. Wall R.L. Aggarwal R.E. Fahey A.J. Strauss	Tunable Solid State Lasers Topical Meeting, Williamsburg, Virginia, 25-28 October 1987
7673	Progress in Single Frequency Ti:Al ₂ O ₃ Lasers	P.A. Schulz S.K. McClung	
7678	Recent Advances in Solid State Laser Technology	A. Mooradian	
7704	Avalanche-Induced Drain-Source Breakdown in Silicon-on-Insulator n-MOSFETs	K.K. Young	1987 IEEE SOS/SOI Technology Workshop, Durango, Colorado, 6-8 October 1987
7714	Multiple-Quantum-Well Structures for Electrooptic Devices	B.F. Aull	Technical Seminar Series, (1) University of Massachusetts, Amherst, 14 October 1987 and (2) Purdue University, 29 October 1987
7723	High-Performance Wideband Superconductive Chirp Filters	M.S. DiIorio* R.S. Withers A.C. Anderson B-Y. Tsaur	1987 Workshop on Superconductive Electronics, Orange County, California, 26-30 October 1987
7724	Process Control for Low-Temperature Deposition of Niobium-Nitride Thin Films	A.C. Anderson D.J. Lichtenwalner W.T. Brogan	

* Author not at Lincoln Laboratory.

ORGANIZATION

SOLID STATE DIVISION

A.L. McWhorter, *Head*
I. Melngailis, *Associate Head*
E. Stern, *Associate Head*
J.F. Goodwin, *Assistant*

N.L. DeMeo, Jr., *Associate Staff*

QUANTUM ELECTRONICS

A. Mooradian, *Leader*
P.L. Kelley, *Associate Leader*
A. Sanchez-Rubio, *Assistant Leader*

Aggarwal, R.L.	McClung, S.K.
Barch, W.E.	Menyuk, N.
Belanger, L.J.	Mims, V.A.*
Brailove, A.A.	Schulz, P.A.
Daneu, V.	Seppala, J.P.
DeFeo, W.E.	Sharfin, W.F.
Fan, T.Y.	Sullivan, D.J.
Hancock, R.C.	Tapper, R.S.
Hryniewicz, J.V.	Walker, W.A.
Jeys, T.H.	Wall, K.F.
Lacovara, P.	Zayhowski, J.J.
Le, H.Q.	

ELECTRONIC MATERIALS

A.J. Strauss, *Leader*
B-Y. Tsaur, *Associate Leader*
H.J. Zeiger, *Senior Staff*

Anderson, C.H., Jr.	Iseler, G.W.
Button, M.J.	Kolesar, D.F.
Chen, C.K.	Krohn, L., Jr.
Choi, H.K.	Mastromattei, E.L.
Clark, H.R., Jr.	Mattia, J.P.
Connors, M.K.	Nitishin, P.M.
Delaney, E.J.	Pantano, J.V.
Eglash, S.J.	Tracy, D.M.
Fahey, R.E.	Turner, G.W.
Finn, M.C.	Wang, C.A.

APPLIED PHYSICS

R.C. Williamson, *Leader*
D.L. Spears, *Assistant Leader*
R.H. Rediker, *Senior Staff*

Aull, B.F.	Hovey, D.L.	Rauschenbach, K.
Betts, G.E.	Johnson, L.M.	Reeder, R.E.
Bossi, D.E.†	Ketteridge, P.A.	Seielstad, D.A.
Corcoran, C.J.†	Kim, S-M.†	Shiple, S.D.†
Cox, C.H., III	Liau, Z.L.	Tsang, D.Z.
Diadiuk, V.	Lind, T.A.	Walpole, J.N.
Donnelly, J.P.	O'Donnell, F.J.	Woodhouse, J.D.
Ferrante, G.A.	Palmacci, S.T.	Yap, D.†
Groves, S.H.	Palmateer, S.C.	Yee, A.C.
Harman, T.C.	Pang, L.Y.†	

* Staff Associate

† Research Assistant

ANALOG DEVICE TECHNOLOGY

R.W. Ralston, *Leader*

R.S. Withers, *Associate Leader*

Anderson, A.C.
Arsenault, D.R.
Bhushan, M.
Boisvert, R.R.
Brogan, W.T.
Denneno, A.P.
Dolat, V.S.
Fitch, G.L.

Frickey, J.M.
Green, J.B.
Holtham, J.H.
Lattes, A.L.
Lichtenwalner, D.J.†
Macedo, E.M., Jr.
Munroe, S.C.
Oates, D.E.

Pan, J.Y.†
Sage, J.P.
Seidel, M.N.†
Slattery, R.L.
Steinbeck, J.W.
Thompson, K.E.
Wong, S.C.†

MICROELECTRONICS

W.T. Lindley, *Leader*

R.A. Murphy, *Associate Leader*

E.D. Savoye, *Associate Leader*

D.J. Ehrlich, *Assistant Leader*

B.B. Kosicki, *Assistant Leader*

Anderson, K.†
Astolfi, D.K.
Bales, J.W.†
Bennett, P.C.
Black, J.G.
Bozler, C.O.
Brown, E.R.
Burke, B.E.
Calawa, A.R.
Chen, C.L.
Chiang, A.M.
Clifton, B.J.
Daniels, P.J.
Doherty, C.L., Jr.
Doran, S.P.
Durant, G.L.
Efremow, N.N., Jr.
Felton, B.J.
Gajar, S.A.†

Geis, M.W.
Goodhue, W.D.
Gray, R.V.
Gregory, J.A.
Hollis, M.A.
Huang, J.C.M.
Johnson, B.W.
Johnson, K.F.
LaFranchise, J.R.
LeCoz, Y.L.†
Lincoln, G.A., Jr.
Lyszczarz, T.M.
Mahoney, L.J.
Maki, P.A.
Manfra, M.J.
Mathews, R.H.
McGonagle, W.H.
McIntosh, K.A.
Melngailis, J.‡

Mountain, R.W.
Nichols, K.B.
Pang, S.W.
Parker, C.D.
Pichler, H.H.
Rabe, S.
Rathman, D.D.
Reich, R.K.
Reinold, J.H., Jr.
Rooks, M.J.
Rothschild, M.
Sedlacek, J.H.C.
Smith, F.W.†
Smythe, D.L., Jr.
Sollner, T.C.L.G.
Uttaro, R.S.
Vera, A.
Wilde, R.E.
Young, E.M.

* Staff Associate

† Research Assistant

‡ Part Time

1. SOLID STATE DEVICE RESEARCH

1.1 MONOLITHIC TWO-DIMENSIONAL SURFACE-EMITTING ARRAYS OF GaAs/AlGaAs DIODE LASERS

Monolithic two-dimensional arrays of GaAs/AlGaAs diode lasers with light emission normal to the surface have been obtained by fabricating edge-emitting quantum-well lasers coupled with external mirrors that deflect the radiation from the laser facets by 90° . Linear arrays of GaAs/AlGaAs devices in which one of the laser facets was cleaved while the other facet and an adjacent 45° deflector were formed by ion-beam-assisted etching¹ (IBAE) have been reported.² For the arrays reported in this section, IBAE was used to form all of the laser facets and the deflecting mirrors. A mass transport process of the type employed to fabricate two-dimensional arrays of GaInAsP/InP lasers coupled with deflecting mirrors³ is not known for AlGaAs.

The GaAs/AlGaAs wafers used for the arrays contained a single quantum well symmetrically positioned in a large optical cavity. Organometallic vapor phase epitaxy was used to grow the following epitaxial layers on a (100) Si-doped n^+ -GaAs substrate: $1.0\text{-}\mu\text{m}$ n^+ -GaAs buffer, $1.0\text{-}\mu\text{m}$ $n\text{-Al}_{0.5}\text{Ga}_{0.5}\text{As}$ confinement, $0.12\text{-}\mu\text{m}$ undoped $\text{Al}_{0.3}\text{Ga}_{0.7}\text{As}$, $0.02\text{-}\mu\text{m}$ undoped $\text{Al}_{0.1}\text{Ga}_{0.9}\text{As}$ active, $0.12\text{-}\mu\text{m}$ undoped $\text{Al}_{0.3}\text{Ga}_{0.7}\text{As}$, $1.8\text{-}\mu\text{m}$ $p\text{-Al}_{0.5}\text{Ga}_{0.5}\text{As}$ confinement, $0.1\text{-}\mu\text{m}$ $p^+\text{-Al}_{0.5}\text{Ga}_{0.5}\text{As}$, and $0.15\text{-}\mu\text{m}$ $p^+\text{-GaAs}$ contacting. The active layer plus the two $0.12\text{-}\mu\text{m}$ undoped $\text{Al}_{0.3}\text{Ga}_{0.7}\text{As}$ layers on either side of the active layer form the large optical cavity.

Two different types of laser arrays have been fabricated. In the first, two deflecting mirrors are formed and light is taken out of both facets of each laser. In the second, only one deflector is formed and a totally reflecting mirror is placed on the back laser facet. The fabrication procedure for the second type of array is much simpler than the first. The design of the first type of laser arrays is shown schematically in Figure 1-1. The first step in fabrication was to etch the laser facets. With photoresist as an etch mask, IBAE was used to form pairs of straight-sided grooves $2\text{ }\mu\text{m}$ wide and about $3\text{ }\mu\text{m}$ deep parallel to the (011) cleavage plane. The distance between the outer walls of the two grooves in each pair is $50\text{ }\mu\text{m}$. The outer walls of each pair form the facets of the laser cavities, which are $250\text{ }\mu\text{m}$ long. Lines about $3\text{ }\mu\text{m}$ wide immediately adjacent to the inner wall of one of the etched grooves in each pair were opened in a new layer of photoresist, and approximately parabolic deflectors for one side of each laser row were formed by IBAE while the angle between the wafer and the ion beam was continuously varied.⁴ The deflector for the other side of each row was formed in a similar manner. A $0.21\text{-}\mu\text{m}$ layer of Si_2N_4 was deposited on the entire wafer by RF-enhanced plasma chemical vapor deposition. Next, $5\text{-}\mu\text{m}$ -wide stripe contact windows on $150\text{-}\mu\text{m}$ centers, oriented normal to the etched facets, were opened in the Si_3N_4 . The wafer was thinned to approximately $75\text{ }\mu\text{m}$, and Ni/Ge/Au contacts were applied to the back side. Two Cr/Au angle evaporations were made to contact the top of the nitride-defined lasers and to coat the deflectors on both sides of each laser row.

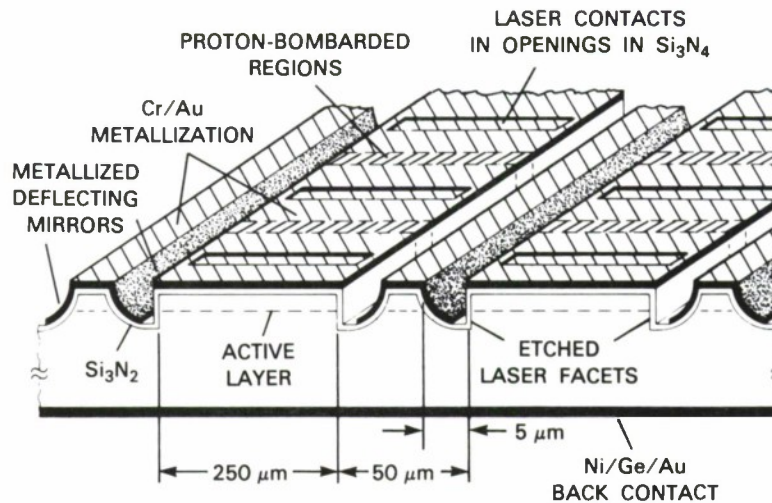


Figure 1-1. Schematic diagram of a monolithic two-dimensional surface-emitting GaAs/AlGaAs diode laser array with light emission from both laser facets of each laser. Arrays with light emission from only one facet of each laser also were fabricated.

During each angle evaporation, the laser facets that otherwise would also have been coated were protected with photoresist. Thick photoresist was deposited on the top of the wafer and stripes approximately $6\text{ }\mu\text{m}$ wide were opened midway between the laser contacts. The wafer was then proton bombarded to introduce sufficient loss between the lasers in each row to suppress lasing in the transverse direction; such lasing had been observed for arrays that were not bombarded. For arrays of the second type, the fabrication procedure is similar, except only one deflecting mirror is etched and a single angle evaporation without masking is used to coat the deflecting mirror, contact the lasers, and form a reflecting mirror on the back (nonemitting) laser facets.

Arrays of the first type with 20-30 laser elements were cleaved from one wafer, mounted for testing and evaluated during pulsed (100-ns pulses, 1-kHz repetition rate) operation. Figure 1-2 shows the near-field pattern taken at about twice threshold for an array consisting of two rows of 11 laser elements each, all bonded in parallel. Since this array had deflecting mirrors on both sides of each laser, the middle spots are each produced by the overlapping outputs from two lasers, one in each row, and are therefore larger than the outside spots. Other arrays from this wafer had similar characteristics.

Figure 1-3 is a plot of the power output vs current for the array whose near-field pattern is shown in Figure 1-2. The sharpness of the knee in the curve shows that the threshold currents of the individual laser elements are fairly uniform. The extrapolated threshold current for the entire array is about 3.5 A, for an average threshold of about 160 mA per laser. The differential quantum efficiency is about 15% at low currents but increases to about 25% at the higher current levels. A power output of 3.7 W, which corresponds to a power density of $\approx 370\text{ W/cm}^2$, was

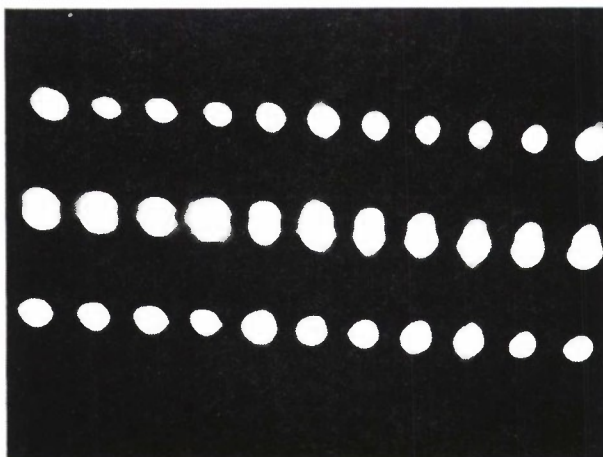


Figure 1-2. Near-field pattern of a 22-element array with light emission from both facets of each laser.

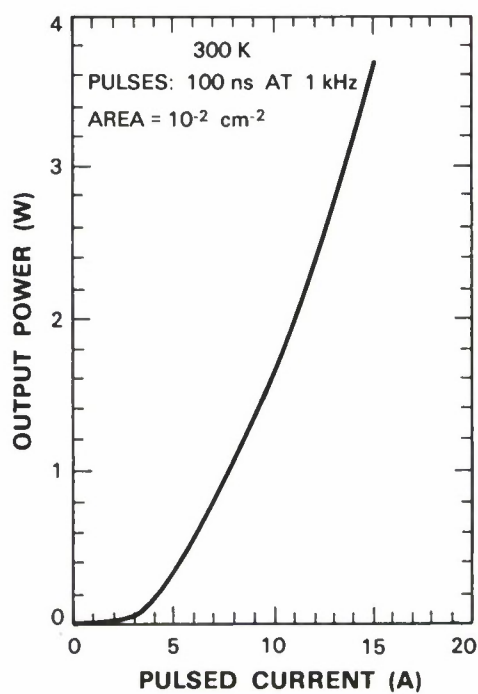


Figure 1-3. Pulsed power output vs current of two-dimensional array whose near-field pattern is shown in Figure 1-2. The current pulses were 100 ns wide at a 1-kHz repetition rate.

obtained at a current of 16 A. Above this level, facet damage occurred on one laser, but the rest of the lasers in the array continued to function. The emission wavelengths of lasers in this array varied from about 790 to 798 nm. This wavelength range is consistent with the active layer composition of $\text{Al}_{0.1}\text{Ga}_{0.9}\text{As}$.

Several large arrays of the second type consisting of approximately 100 elements each were cleaved from another wafer. Figure 1-4 shows the near-field pattern of a 96-element array at about 1.25 times threshold. On this wafer, light is taken out of only one facet of each laser. As can be seen, all 96 elements lase. This was true for most of the large arrays fabricated. A pulsed

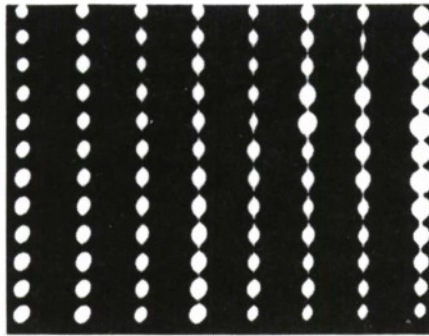


Figure 1-4. Near-field pattern of a 96-element array with light emission from only one facet of each laser.

power output of 7 W, limited by available current, was obtained from this array. Higher powers are anticipated when higher current capabilities become available. The differential quantum efficiencies on these large arrays, however, were only 8-10%. Significant improvements in quantum efficiency, as well as threshold current and power output, are anticipated through improvements in material quality, laser design, and fabrication procedures.

J.P. Donnelly	T.H. Windhorn
W.D. Goodhue	R.J. Bailey

1.2 INTEGRATED OPTICS WAVEFRONT MEASUREMENT SENSOR

Sensors consisting of an array of interferometers to measure phase differences and straight waveguides to measure intensity along an optical wavefront have been fabricated on LiNbO_3 at four wavelengths ($\lambda = 0.458, 0.514, 0.82, \text{ and } 3.39 \mu\text{m}$), and the performance of the sensors has been evaluated.⁵ The outputs of the arrays are coupled to an imaging CCD and fed into a computer. In this report, we describe the demonstration of short-frame-time operation in which ten 200-ns snapshots have been taken of a $0.514\text{-}\mu\text{m}$ collimated wavefront that has been acousto-optically tilted at the sensor aperture during a $2\text{-}\mu\text{s}$ interval.

The experimental arrangement used for measurements at $0.514\ \mu\text{m}$ is shown in Figure 1-5. At the upper left-hand corner is the argon ion laser. The laser beam is attenuated by two banks of neutral density filters, and then passes through a polarizer so it can be oriented either TE or TM when it is incident on the waveguides. (The laser beam is oriented at 45° to both polarizations before the polarizer.) A beam splitter splits off a small portion of the energy to an input beam monitor. A beam expander with a spatial filter both expands the beam and removes aberrations so a collimated beam of about 5-cm diameter with a nearly perfect flat wavefront is incident on the integrated optics wavefront measurement sensor (IOWMS). The circular inset shows the acousto-optic (AO) cell that is used to deflect and tilt the first-order beam incident on the IOWMS. It also is used simultaneously as a shutter to reduce the duty cycle of the incident radiation on the IOWMS. For a $2\text{-}\mu\text{s}$ sweep, the beam deflection of the AO cell was linear in time over an angular range of about 2.5 mrad, which corresponds to a 45° range of phase tilts across the interferometer arms (separation = $26\ \mu\text{m}$). During each $2\text{-}\mu\text{s}$ sweep, ten frames of data were obtained.

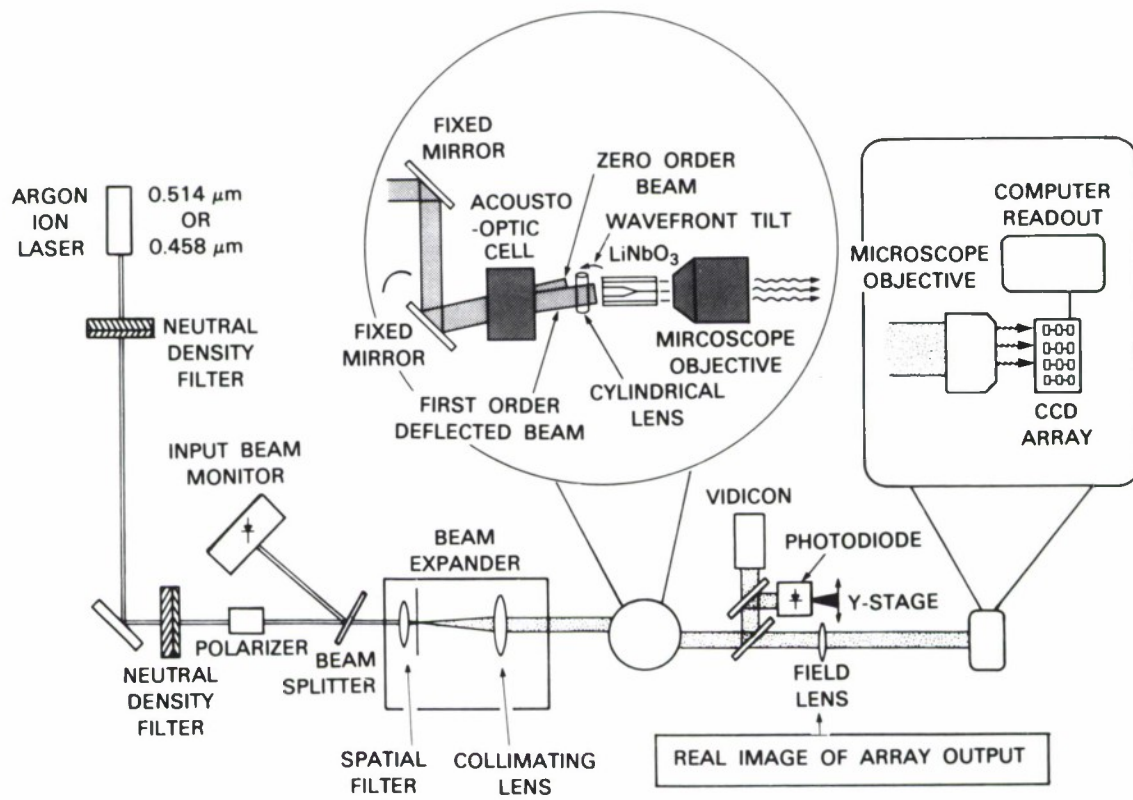


Figure 1-5. The experimental arrangement for high-temporal-resolution measurements at $\lambda = 0.514\ \mu\text{m}$ in which the wavefront is tilted by means of an acousto-optic cell.

The outputs of the waveguides are focused by a $5\times$ microscope objective to produce a real image. Another $5\times$ microscope objective is used at the CCD the same distance from the real image, so the optical train between the output of the waveguides in the LiNbO_3 and the imaging CCD cells has a 1-to-1 magnification. A field lens of focal length $d/4$, where d is the distance between the two objectives, is placed in the plane of this real image to prevent vignetting (to assure the collection of off-axis light from the first microscope objective at the second microscope objective). A flip mirror is in the optical path between the waveguide array and the CCD, so the waveguide output can be imaged if desired at the vidicon instead of at the field lens. A second flip mirror is shown that imaged an individual waveguide output onto a photodiode that could be translated in 41 discrete steps to obtain the data from the 41 guides for diagnostic purposes.

The CCD and the microscope objective that focuses the light on the CCD imaging cells are shown schematically in the rectangular inset in Figure 1-5. The CCD was a polysilicon gate, front-illuminated, buried-channel device consisting of 64 columns by 128 rows of cells. The CCD had one imaging row and the next ten rows were used to store the ten frames. The CCD support circuitry placed a lower limit of 200 ns on the clock time and thus on the frame time. The stored data were read out of the device at a 1-MHz rate.

The data from the experiment are presented in Figure 1-6. For the flat wavefront being tilted at the input to the IOWMS, all the interferometer resolution elements should yield the same value for the phase angle θ (or its equivalent tilt angle), given on the abscissa of Figure 1-6. Plotted in Figure 1-6 are the measurement errors (deviations from expected values) for 10 of the 20 interferometers for ten 200-ns-duration measurements during the 2- μs -duration deflection by the AO cell. Note that these phase errors are less than $\pm \lambda/50$. The general trend of an increase in phase error from $\theta = -100^\circ$ to $\theta = -55^\circ$ suggests a systematic error in the calibration of the AO deflection. In obtaining the data of Figure 1-6, there was a limited power density available at the interferometer array from the argon ion laser beam after it had been spatially filtered and expanded to give a flat wavefront with reasonably uniform intensity over the array. Because of this limited power density, there were less than 1800 signal electrons in a charge packet collected in the 200-ns integration time. From statistical analysis of the operation of the IOWMS and this knowledge of the number of electrons, the value of the standard deviation in the phase angle $\sigma(\theta)$ is calculated to be 1.0° of phase for $\theta = -100^\circ$ and 1.5° for $\theta = -55^\circ$. The value of $\sigma(\theta)$ for the 100 data points in Figure 1-6 is 3.0° , which is in reasonable agreement with these predictions.

The data presented in Figure 1-6 indicate that the errors in the phase measurement are very small. Thus the IOWMS is useful in evaluating the flatness of the wavefront from both CW and pulsed lasers, lenses, mirrors, and other optical components. In addition, the high temporal resolution of the IOWMS demonstrated by the 200-ns frame time used to obtain the data will make possible the investigation of high-frequency phenomena.

R.H. Rediker
T.A. Lind
B.E. Burke

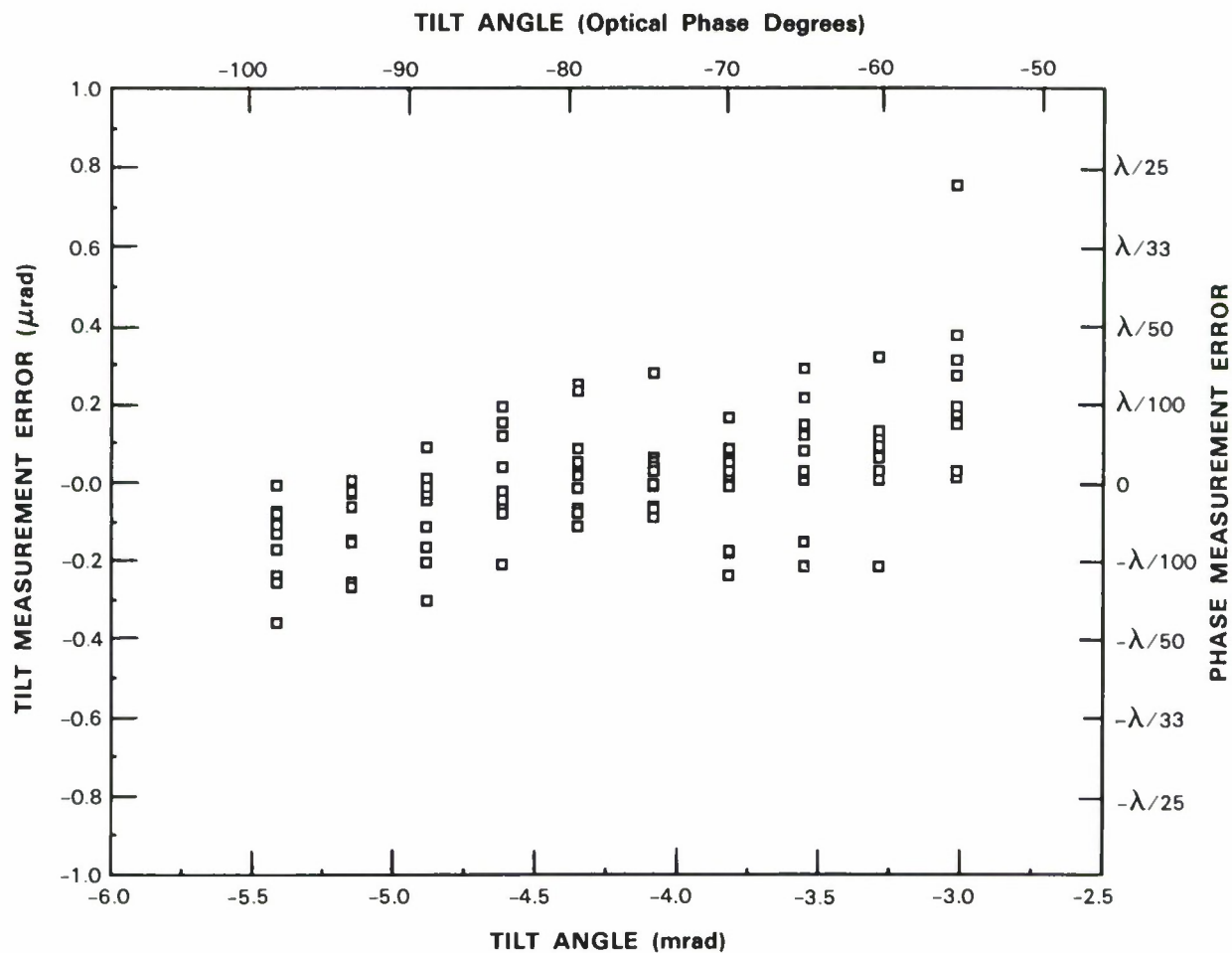


Figure 1-6. Tilt measurement errors for ten 200-ns-duration measurements taken as the acousto-optic cell tilts the wavefront at the IOWMS by 2.5 mrad (corresponding to 45° of phase) in $2 \mu\text{s}$. These errors are due in large part to the statistics associated with the limited number of electrons in the CCD imager charge packets.

1.3 STABILIZATION OF THE OPTICAL POWER OF A LASER DIODE

It is relatively straightforward to design an electrical feedback loop⁶ that stabilizes the optical output from a semiconductor laser diode at a particular level. Achieving a stabilized output over a range of optical powers is complicated by the fact that several of the laser's optical and electro-optical parameters that affect feedback loop design are functions of the laser operating point. Variation in these parameters is particularly strong, e.g., changes of the order of 100, when the range of stabilized optical powers extends both above and below the laser threshold. The basis for this variation is the change in the dominant emission mechanism around the threshold: spontaneous below and stimulated above. Variation in an optical parameter, examples of which are beam intensity and state of polarization, requires that the feedback loop monitoring configuration must be chosen such that the variation has the same effect on both the usable and monitored beams. Variation in an electro-optical parameter, such as differential quantum efficiency, results in a loop transmission that is dependent upon the laser operating point. Consequently, the feedback loop must be designed so that key performance parameters, such as stability and speed of response, remain within acceptable limits over the full range of parameter variation.

A specific application of the above general discussion is the stabilization of the optical power in the core mode of a single-mode fiber, independent of the state of polarization, over a range in powers both above and below laser threshold.

The common monitoring configuration, which uses a large-area photodiode mounted behind the back face of a fiber-coupled laser diode, is fundamentally unsuitable in this application, since the signal from such a photodiode is proportional to beam irradiance. A signal proportional to beam intensity can be obtained by using a fiber-optic splitter to tap off a portion of the optical power in the laser's output fiber. In addition, this monitor configuration will provide compensation for changes in the laser-to-fiber coupling efficiency, since this coupling is now inside the feedback loop. The cladding-mode power can be reduced to insignificant levels with a cladding-mode stripper. However, it must be inserted before the fiber-optic monitor splitter, since the splitting ratio of fiber-optic splitters is not in general the same for cladding as for core modes.

The magnitude of the loop transmission is directly dependent upon the differential quantum efficiency. As long as a fixed response time (the time required for a change in control level to result in a new optical power level) is not required, this problem can be handled easily by designing a feedback loop that has the required degree of stability at the maximum loop transmission. Consequently, the loop will be stable for lower loop transmission magnitudes, but the response time will be correspondingly slower.

A block diagram of a feedback loop that incorporates all of the above features is shown in Figure 1-7. A standard, commercially available fiber-coupled laser capable of launching 1.0 mW of 1.3- μm optical power into a single-mode optical fiber was used. The mode stripper was implemented by winding approximately 10 m of single-mode fiber around a 5-cm-diameter

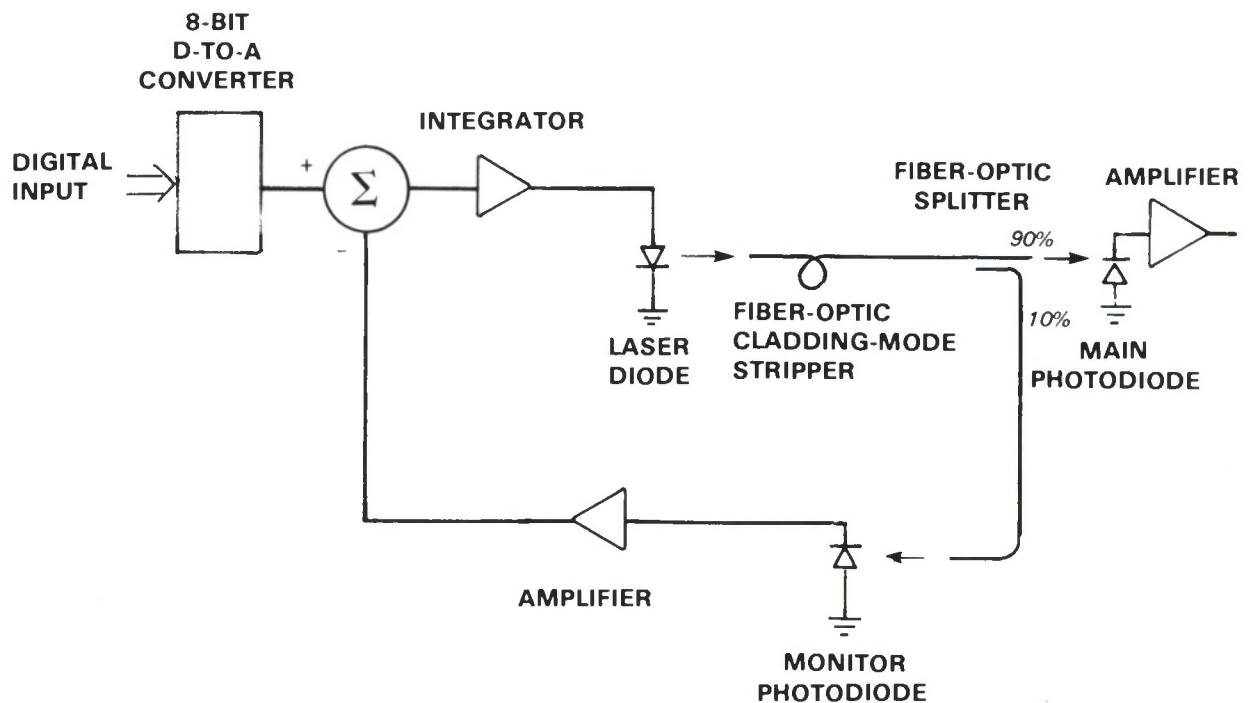


Figure 1-7. Block diagram of the experimental setup for controlling the optical power from a semiconductor laser diode at operating points both above and below the laser threshold.

cylinder. A commercially available fiber-optic power splitter was used to divide the optical power into the usable (90%) and monitor (10%) fibers. Each of these fibers was coupled to one of the two identical, fiber-coupled photodetectors, also standard commercial components. The digital input that corresponds to the desired optical power level was converted to analog form via an 8-bit digital-to-analog converter (DAC). The choice of 8 bits for the word length is not crucial to the experiment; among the selection criteria were the fact that 8 bits would require operation above and below threshold, represent a potentially useful range, and avoid being cumbersome to implement. The DAC output was compared to an appropriately amplified signal from the monitor photodiode. The difference was integrated by an operational amplifier whose output fed the transistor that controls the current through the laser. The integrator time constant was chosen so that it was the dominant time constant in the feedback loop. The dc loop gain was chosen so that with the maximum differential quantum efficiency the loop had at least 90° of phase margin; thus, when the loop is operating at a point where the efficiency is less, the gain will be lower and the phase margin will approach 180°.

The control system was evaluated by measuring the output from the main photodetector as a function of the input setting to the DAC. A concise way to test the performance of the loop over its entire range is to turn on each bit individually. Ideally, this should produce a binary

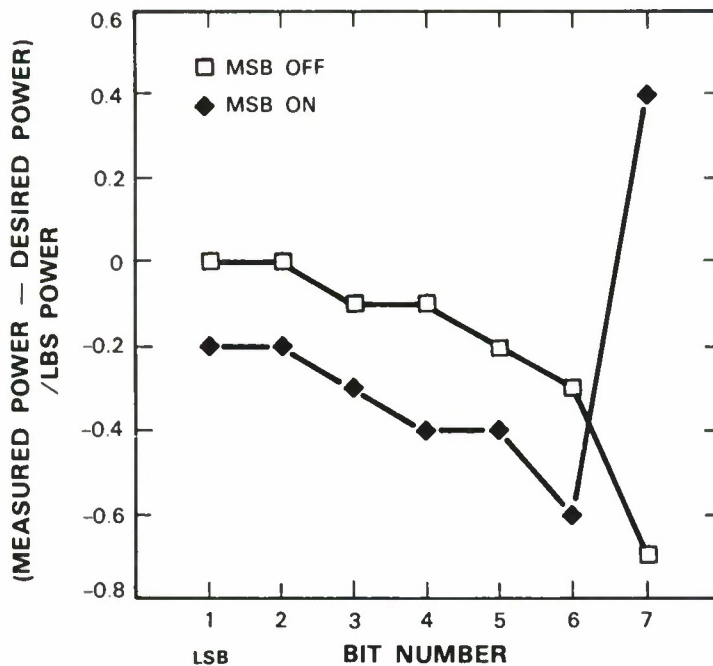


Figure 1-8. Performance of implementation shown in Figure 1-7. The difference between the measured and calculated optical power levels, normalized by the power in the least significant bit (LSB) is plotted vs the bit number, activated individually. Data were taken with the most significant bit (MSB) off and on.

progression of optical powers. Further, by repeating this measurement, once with the most significant bit (MSB) off and then with the MSB on, it is possible to compare directly the performance of the loop about two operating points, one below and one above threshold. Figure 1-8 is a plot of the data from such a measurement. The abscissa is the bit number; the ordinate is the difference between the measured value of the optical power and an ideal binary progression of optical powers, normalized by the optical power of the least significant bit (LSB). Note that the general shape of the error curves is the same with the MSB off and on. This suggests that the operating-point-induced errors have been reduced to the point where they are negligible compared with the errors in the feedback loop and DAC. Further note that all the errors are less than one LSB, and at low powers the errors are less than 0.1 LSB.

C.H. Cox, III

REFERENCES

1. G.A. Lincoln, M.W. Geis, S. Pang, and N.N. Efremow, J. Vac. Sci. Technol. B **1**, 1043 (1983).
2. T.H. Windhorn and W.D. Goodhue, Appl. Phys. Lett. **48**, 1675 (1986).
3. Z.L. Liao and J.N. Walpole, Appl. Phys. Lett. **50**, 528 (1987).
4. W.D. Goodhue, G.D. Johnson, and T.H. Windhorn, in *Gallium Arsenide and Related Compounds 1986*, edited by W.T. Lindley (Inst. Phys. Conf. Ser. 83, Bristol, England, 1987), p. 349.
5. Solid State Research, Lincoln Laboratory, MIT (1985:4), pp. 2-5, DTIC AD-A172872.
6. J.K. Roberge, *Operational Amplifiers: Theory and Practice* (Wiley, New York, 1975).

2. QUANTUM ELECTRONICS

2.1 SYNCHRONOUSLY PUMPED MODE-LOCKED Ti:Al₂O₃ LASER

We have demonstrated synchronously pumped mode-locked laser operation in a Ti:Al₂O₃ ring laser. The laser pump source was a frequency-doubled Nd:YAG laser-amplifier system producing a 60- μ s-long macropulse that comprised a wavetrain of mode-locked 70-ps micropulses with a 10-ns spacing (100 MHz).

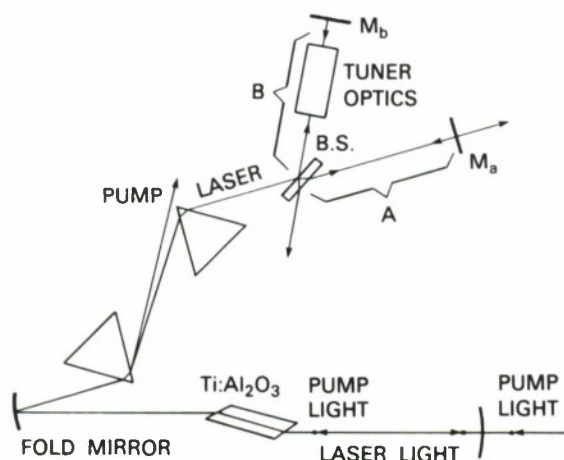
The Ti:Al₂O₃ laser consisted of a 1-cm-long crystal with faces cut at the Brewster angle and placed in a ring laser cavity configuration with a 2% output coupling mirror. The cavity was adjusted for a 5-ns round trip transit time, which was close to half the temporal spacing of the pump pulse. When the crystal was pumped synchronously at 532 nm with a 30-mJ macropulse, which was approximately an order of magnitude above the laser threshold, mode-locked lasing at \sim 200 MHz was obtained. This macropulse pump energy corresponds to an average micropulse pump energy of about 5 μ J at the Ti:Al₂O₃ crystal face. The mode-locked operation of the Ti:Al₂O₃ was observed only after several microseconds into the macropulse, indicating a long build-up process over many cavity trips. During this time, relaxation oscillations were observed. When mode locking started, the relaxation oscillation frequency increased by an order of magnitude.

Synchronous pumping has been limited to operation with dye lasers and used either a CW¹ or pulsed² mode-locked pump source. Recent work³ has demonstrated CW mode-locked operation of a Ti:Al₂O₃ laser. Our result raises the possibility that pulsed synchronous pumping may be used to obtain significantly narrowed laser pulses in Ti:Al₂O₃

P.A. Schulz
N. Menyuk
M.E. MacInnis

2.2 TUNING EXPERIMENTS ON A Ti:Al₂O₃ LASER USING AN INTERFEROMETRIC CAVITY

Work on the Ti:Al₂O₃ master oscillator has continued in the direction of finer wavelength selectivity in the electro-optic tuning system. As more intracavity optical components are added to the tuner, the increase in lasing threshold due to the additional insertion losses tends to become excessive; for instance, a two-stage Lyot filter of the type previously described, when inserted into the laser cavity, brings the threshold pump power to approximately 10 W, compared with 4 W for the 'bare' cavity. It also has been noticed that extended CW operation of the LiNbO₃ tuning crystals with high voltages applied gives rise to objectionable photorefractive phenomena, resulting in a substantial increase in lasing threshold over a period of about 1 h. Both problems can be solved effectively by moving the tuning optics from the main laser cavity to a weakly coupled side arm, as shown in Figure 2-1. The beam splitter reflects approximately 3% of the main intracavity intensity into the side arm; this loss is sufficient to prevent lasing at



92044-8

Figure 2-1. Laser cavity geometry. B.S. is a beamsplitter, coated on one side with a 3% reflecting thin film; the opposite side is used at Brewster's angle.

the pump power level used, unless the two waves returning along arms A and B interfere destructively at the beam splitter output (see Figure 2-1). The resonance condition for the configuration shown is analogous to that of a Michelson interferometer⁴; since only a small fraction of the intensity is coupled into arm B, the effect of losses in this arm is correspondingly reduced, while still maintaining the frequency-selecting action of the tuning optics. At the same time, the reduced light intensity in arm B makes the LiNbO₃ photorefractive effect not observable over a period of a few hours. With the arrangement of Figure 2-1, tuning can be obtained over most of the Ti:Al₂O₃ gain curve, similar to previously reported results.⁵ A two-stage electro-optic filter inserted in arm B causes an increase in lasing threshold of only about 1 W.

The timing requirements for the agile beam allow up to 1 ms for large wavelength shifts, while smaller jumps within a narrow range must occur on a microsecond scale. This suggests the use of a mixed electro-optic-mechanical approach to the tuner design, which may simplify the required optics. One geometry is shown in Figure 2-2; the insertion of a Brewster-angle prism in arm B allows mechanical tuning by adjusting the orientation of the end mirror, M_b. For a fused silica prism, the angular motion required of the mirror for a 200-nm tuning range is 0.3°. The oscillation bandwidth allowed by the prism-mirror combination is of the order of a nanometer; within this bandwidth, the desired wavelength can then be selected electro-optically. The advantage over an all-electro-optic design is that the free spectral range requirement for the birefringent tuner is reduced by two orders of magnitude. Although this has not been verified yet, it is possible that just one stage of electro-optic tuning with sufficient birefringent bias could be used to select a single cavity mode.

The speed of response of the mechanical tuning has been investigated. In the experiment, mirror M_b is a small glass flat, 5 × 7 × 2 mm in size, coated with a reflecting multilayer and

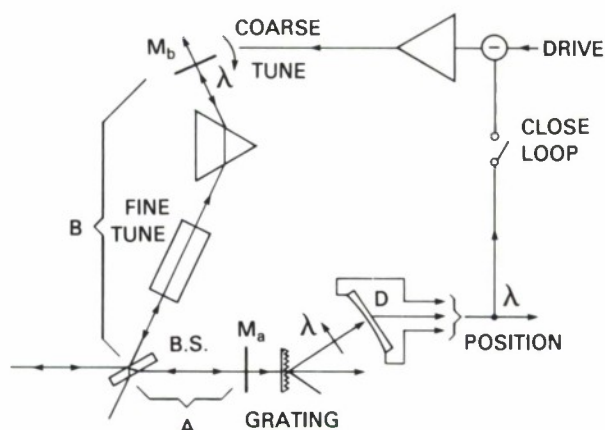


Figure 2-2. Combined mechanical-electro-optic tuning. *D* is a position-sensing silicon photodiode.

mounted on a galvanometer-type scanner. The time behavior of the laser wavelength when the mirror is driven with a step waveform can be determined in the usual manner by sending the laser beam, after diffraction by a grating, to a position-sensing detector, as shown in Figure 2-2. The tuning transient shown in the upper trace of Figure 2-3 exhibits considerable ringing due to the mechanical response of the mirror drive. Better damping and faster response time could be obtained with a galvanometer drive of optimum mechanical design; however, using the wavelength signal from the position sensor in a simple error-correcting servo loop (Figure 2-2) already yields a more satisfactory response, as shown by the lower trace in Figure 2-3.

V. Daneu

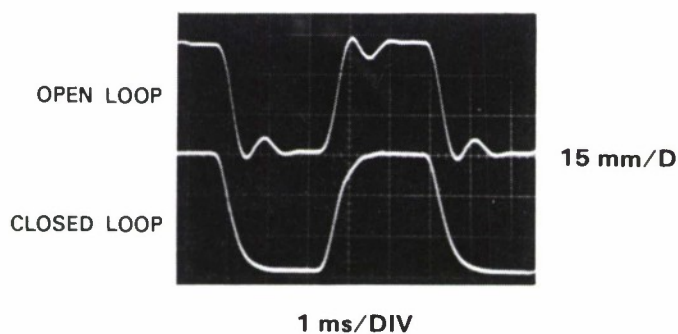


Figure 2-3. Wavelength transient response to a square-wave drive applied to the tuning mirror. Upper trace: open loop response. Lower trace: with feedback from wavelength-sensing detector (Figure 2-2).

2.3 SMALL-SIGNAL GAIN MEASUREMENTS IN A $\text{Ti:Al}_2\text{O}_3$ AMPLIFIER

Small-signal gain measurements have been made on a $\text{Ti:Al}_2\text{O}_3$ amplifier using a CW He-Ne laser or a CW $\text{Ti:Al}_2\text{O}_3$ laser as the signal source. Measurements were made of both single- and double-pass gain. The temporal dependence of the amplified signal as a function of incident pump energy density also was measured.

A schematic of the setup for gain measurements is shown in Figure 2-4. The 532-nm pump beam (10-ns pulses) propagates perpendicular to the c-axis within the $\text{Ti:Al}_2\text{O}_3$ amplifier crystal

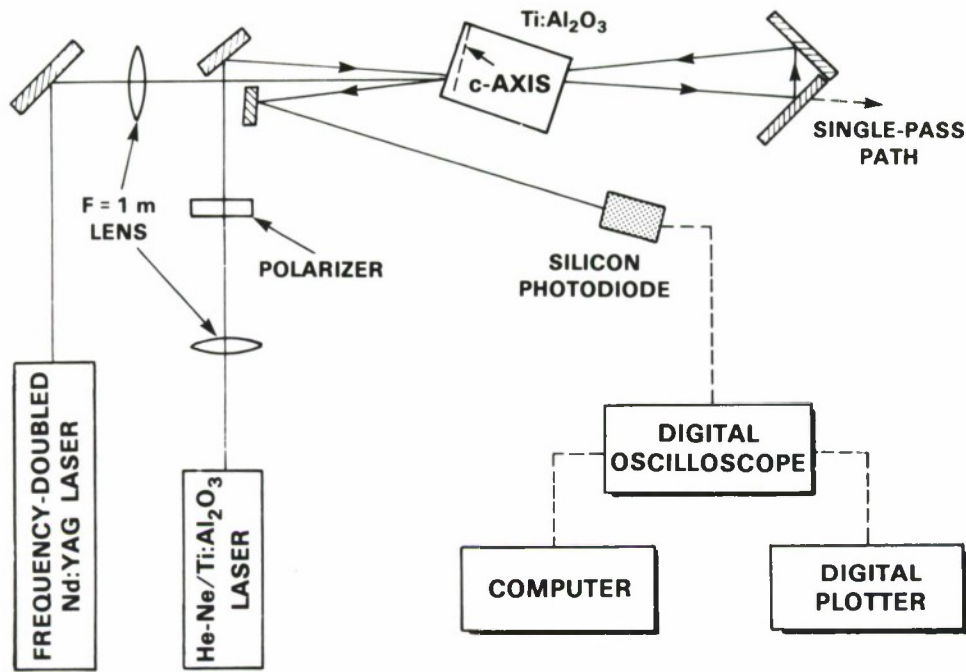


Figure 2-4. Schematic of the experimental setup for the measurement of small-signal double-pass gain in a $\text{Ti:Al}_2\text{O}_3$ amplifier. A frequency-doubled Nd:YAG laser served as the pump source and either a CW He-Ne laser or a CW $\text{Ti:Al}_2\text{O}_3$ was used as the signal source. Single-pass measurements were made along the indicated path with the tuning mirrors removed and the detector repositioned.

with the pump polarization vector parallel to the c-axis. The signal beam from a CW He-Ne laser (632.8 nm) or a single-frequency, CW $\text{Ti:Al}_2\text{O}_3$ laser⁶ (750-850 nm) propagates almost collinearly ($\sim 1^\circ$ angle) with the pump beam.

The $\text{Ti:Al}_2\text{O}_3$ amplifier crystal was an as-grown sample cut from a boule grown by the gradient-freeze technique⁷ at Lincoln Laboratory. The length L of this crystal was 2.1 cm. The 1.1×1.2 -cm entrance and exit faces were polished but uncoated, and the remaining faces were roughly polished. The c-axis was not in the plane of the entrance and exit faces but was rotated $\sim 11^\circ$ from them. In order for the direction of propagation of the pump and signal beams within

the crystal to be essentially normal to the c-axis, their angle of incidence was set to $\sim 20^\circ$. This configuration inhibited parasitic oscillations between the two faces.

The pump-induced intensity of the signal beam is given by

$$I(t) = I_{dc}[e^{g(t)L} - 1] \quad , \quad (2-1)$$

where I_{dc} is the dc signal intensity, $g(t)L$ is the time dependent small-signal gain, and $t = 0$ is defined as the time at which the maximum small-signal gain g_0L occurs. Figure 2-5 shows the exponential gain factor g_0L as a function of incident pump energy density E_p with a $\text{Ti:Al}_2\text{O}_3$ laser used as the signal source. The lower curve shows a single-pass gain in the π polarization (parallel to the c-axis) at 790.7 nm. The maximum exponential gain for the single-pass arrangement was $g_0L = 5.2$ with a corresponding power gain $G_0 \equiv \exp(g_0L) \approx 180$. Comparing this with the He-Ne data, we find that the value of g_0 at 632.8 nm is $\sim 1/25$ that at 790.7 nm, a wavelength close to the peak of the gain profile. The upper curve presents data obtained by double passing the same $\text{Ti:Al}_2\text{O}_3$ amplifier crystal at 799.8 nm in the π polarization. The maximum value of g_0L in this case was 9.2, corresponding to $G_0 \approx 10^4$. No parasitic oscillations were observed in either the single- or double-pass experiment. The straight lines in Figure 2-5 were obtained by a linear fit to the data with the constraint that they pass through the origin.

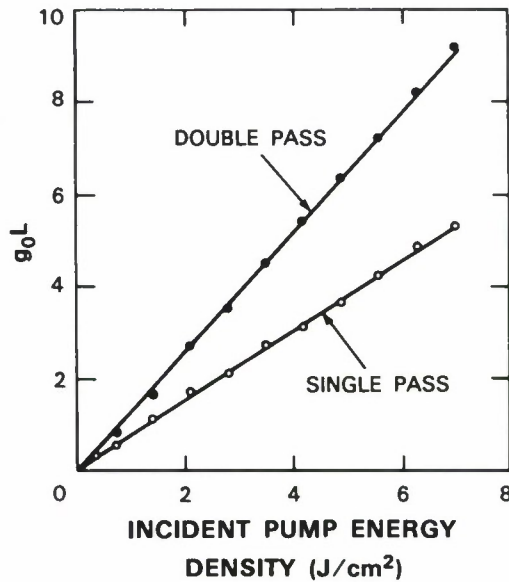


Figure 2-5. The exponential gain g_0L as a function of incident pump energy density for the single- and double-pass experiments at 790.7 nm and 799.8 nm, respectively, with a $\text{Ti:Al}_2\text{O}_3$ laser used as the signal source. The lines through the data are linear fits with the constraint that they pass through the origin.

From the single-pass gain measurements of 790.7 nm, we can estimate the gain cross section at the peak of the gain profile. If we assume that all of the pump photons are absorbed by the Ti^{3+} ions, the gain cross section is given by $\sigma_e = (h\nu_p/E_p)g_oL$ where $h\nu_p$ is the energy of a pump photon. Using $h\nu_p = 2.33$ eV, $E_p = 7$ J/cm², and $g_oL = 5.2$ for the π polarization at 790.7 nm, we find $\sigma_e = 2.8 \times 10^{-19}$ cm². Correcting for the reflection loss of the pump beam at the input face of the crystal yields $\sigma_e = 3.0 \times 10^{-19}$ cm², in agreement with previously published values.⁸⁻¹⁰

To determine the gain anisotropy between the π and σ polarizations (σ is perpendicular to the c-axis), a half-wave plate was inserted between the polarized He-Ne laser and the $\text{Ti:Al}_2\text{O}_3$ amplifier crystal, and g_oL was measured as a function of angle θ between the polarization vector of the He-Ne laser and the c-axis. The dependence of g_oL on $\sin^2\theta$ for $E_p = 3.7$ J/cm² is shown in Figure 2-6. The data are fit very well by a straight line consistent with the equation $g_o = g_\pi - (g_\pi - g_\sigma)\sin^2\theta$ where g_π and g_σ are the gains for the π and the σ polarizations, respectively. From this line, the ratio g_π/g_σ is found to be 2.3.

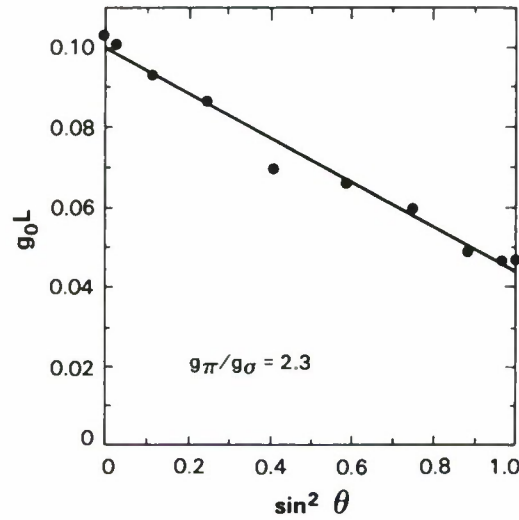


Figure 2-6. The gain anisotropy between the π and σ polarizations at 632.8 nm. The angle between the polarization vector of the He-Ne laser and the c-axis is θ . The straight line is a linear fit of the data to the equation $g_o = g_\pi - (g_\pi - g_\sigma)\sin^2\theta$. The incident pump energy density was 3.7 J/cm².

The decay of the amplified signal $I(t)$ was measured to obtain the pulse width $t_{1/e}$, which is defined as the time required for the signal density to reach $1/e$ of its value at $t = 0$. The value of $t_{1/e}$ was found to decrease with increasing pump energy density. The data points in Figure 2-7 show this decrease for the single-pass experiment at 790.7 nm.

For the small-signal gain regime, in the absence of amplified spontaneous emission, the value of $t_{1/e}$ is given by

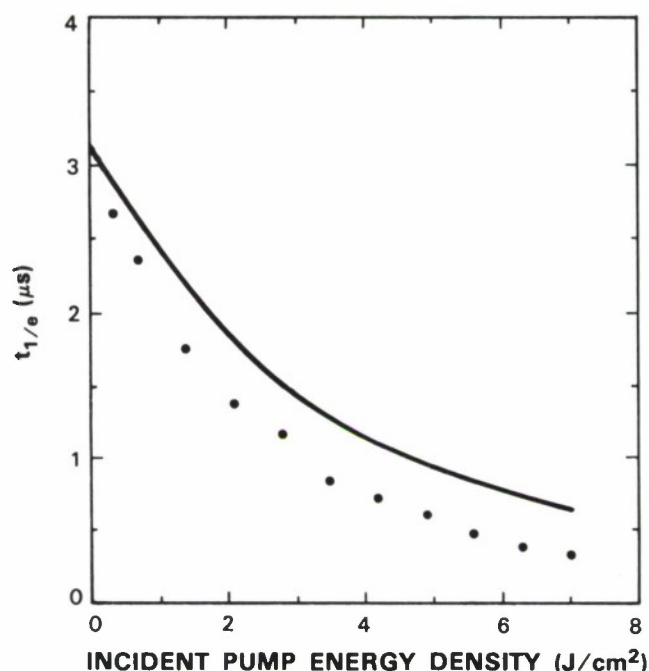


Figure 2-7. The observed pulse width $t_{1/e}$ at 790.7 nm as a function of incident pump energy density. The time required for the signal intensity to reach $1/e$ of its value at $t = 0$ is defined as $t_{1/e}$. The data are indicated by the circles, while the solid line is given by Equation (2-2).

$$t_{1/e} = \tau \ln \left\{ g_0 L / \ln[(e^{g_0 L} - 1)e^{-1} + 1] \right\}, \quad (2-2)$$

where τ is the spontaneous lifetime at room temperature. The solid line in Figure 2-7 was calculated from Equation (2-2) by using the fitted single-pass values for $g_0 L$ in Figure 2-5 and the published value⁸ of 3.15 μ s for τ . The measured values of $t_{1/e}$ lie below the calculated line, probably as a result of amplified spontaneous emission.

K.F. Wall	R.L. Aggarwal
R.E. Fahey	A.J. Strauss

2.4 LIDAR OBSERVATION OF THE EARTH'S SODIUM LAYER

A layer of atomic sodium vapor naturally occurs at an altitude of 90 km above the earth's surface. This sodium vapor has a peak density of 10^3 to 10^4 atoms per cubic centimeter over a 10-km altitude range and is believed to be deposited into the atmosphere by meteoric ablation.¹¹ The spatial and temporal characteristics of this layer have been studied extensively by resonantly backscattering pulsed-dye-laser radiation from the sodium layer.¹² These studies have shown that the sodium layer is a convenient medium for the investigation of upper-atmospheric waves.¹³

For some applications, such as a shuttle-based lidar system,¹⁴ the use of dye lasers is inappropriate. By sum-frequency mixing the output of two Nd:YAG lasers, we have generated a new source of sodium-resonance radiation¹⁵ that has several potential advantages over dye lasers. These advantages include greater high-power reliability, better beam-pointing stability, near diffraction-limited beam quality, and the requisite temporal and spectral properties consistent with efficient use of the available sodium atoms.

The sodium-resonance radiation has been generated by sum-frequency mixing the output radiation of two simultaneously Q-switched Nd:YAG lasers, one operating at $1.064\ \mu\text{m}$ and the other operating at $1.319\ \mu\text{m}$.¹⁵ The Nd:YAG lasers both were operated at a pulse repetition rate of 1 kHz with pulse lengths of about 150 ns and average powers of about 900 mW. The sodium-resonance radiation was generated in a crystal of lithium niobate and had an average output power of about 400 mW, a pulse length of 100 ns, and a spectral range of 2 GHz. Figure 2-8 is a schematic of the sodium-fluorescence-detection apparatus. The sodium-resonance radiation was

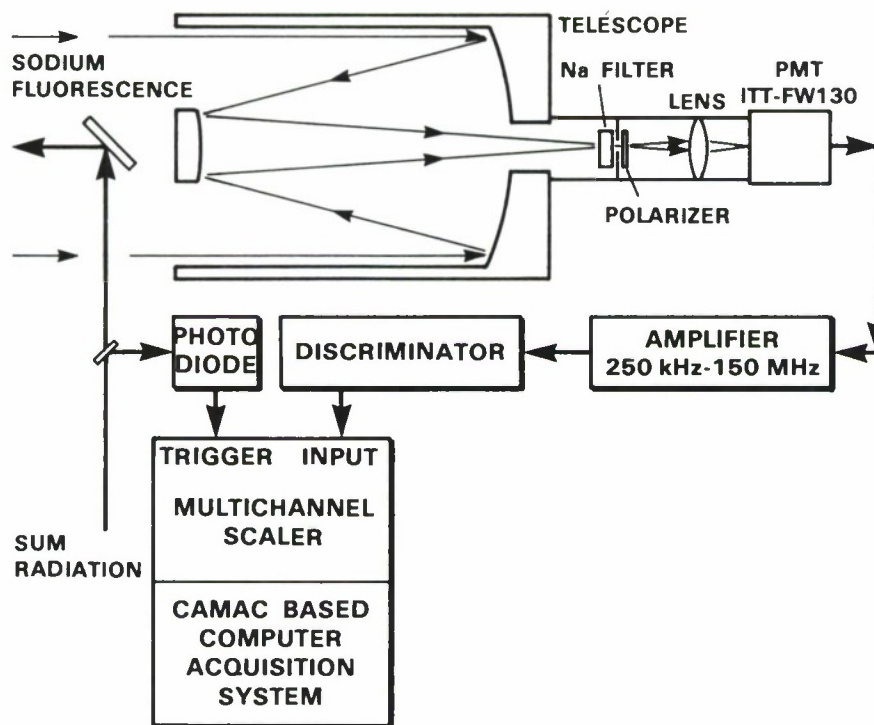


Figure 2-8. Schematic of the sodium-fluorescence-detection apparatus.

transmitted into the atmosphere coaxially with the direction of the receiving telescope which was oriented to zenith. This telescope had an aperture of 583 cm^2 and a field-of-view slightly larger than the 1-mrad divergence of the output sodium-resonance radiation beam. The radiation backscattered by the earth's atmosphere was collected by the telescope and passed through a 0.5-nm-bandwidth interference filter and polarizer. This radiation then was imaged onto the

10^{-3}-cm^2 photocathode of a photomultiplier tube. The photomultiplier counts were recorded by a multichannel scaler as a function of the elapsed time after the sodium-resonance radiation was transmitted into the atmosphere.

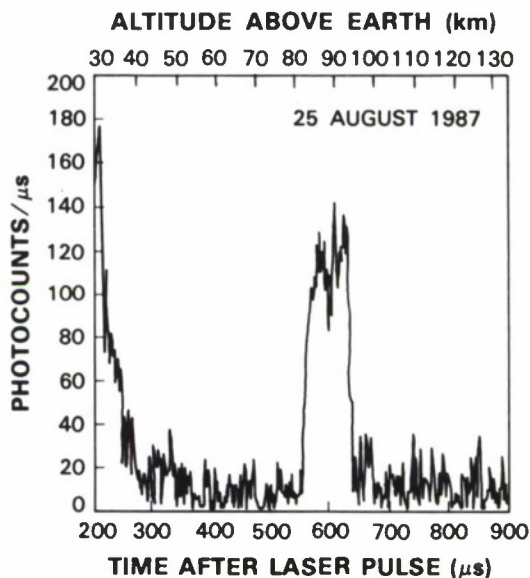


Figure 2-9. Sodium-resonance radiation backscattered by the earth's atmosphere. Photomultiplier counts per microsecond integrated over 2×10^6 laser pulses are plotted as a function of the elapsed time after the sodium-resonance-radiation pulse is transmitted into the atmosphere. The signal from the sodium layer occurs at a round-trip time of $600 \mu\text{s}$.

Figure 2-9 shows the signal received from the earth's upper atmosphere. The signal at early times results from Rayleigh scattering in the atmosphere, while the peak at $600 \mu\text{s}$ corresponds to resonant backscattering from the sodium layer. These data were taken by integrating all the photocounts received over a one-half-hour time span during the evening of 25 August 1987. By using a cooled large-area-photocathode photomultiplier, we hope to achieve noise levels similar to those produced by the small-area-photocathode photomultiplier, and also to achieve much higher signal levels with a less alignment-sensitive detector.

T.H. Jeys
A.A. Brailove
W.E. DeFeo

REFERENCES

1. J. Chesnoy and L. Fini, *Opt. Lett.* **11**, 635 (1986).
2. G. Angel, R. Gagel, and A. Laubereau, *Opt. Commun.* **63**, 259 (1987).
3. J.T. Darrow and R.K. Jain in *Post-deadline Paper Digest of the Topical Meeting on Tunable Solid State Lasers* (Optical Society of America, Washington, D.C., 1987), Paper PD2.
4. P.W. Smith in *Single-Frequency Lasers*, edited by A.K. Levine and A.J. DeMaria (Marcel Dekker Incorporated, New York, 1976).
5. V. Daneu and A. Sanchez, in *Digest of the 1987 Conference on Lasers and Electro-Optics* (Optical Society of America, Washington, D.C., 1987), p. 296.
6. Solid State Research, Lincoln Laboratory, MIT (1987:2), p. 15.
7. R.E. Fahey, A.J. Strauss, A. Sanchez, and R.L. Aggarwal, in *Tunable Solid-State Lasers II*, edited by A.B. Budgor *et al.* (Springer-Verlag, New York, 1986), p. 82.
8. P.F. Moulton, *J. Opt. Soc. Am. B* **3**, 125 (1986).
9. W.R. Rapoport and C.P. Khattak, in *Tunable Solid-State Lasers II*, edited by A.B. Budgor *et al.* (Springer-Verlag, New York, 1986), p. 212.
10. P. Albers, E. Stark, and G. Huber, *J. Opt. Soc. Am. B* **3**, 134 (1986).
11. E.S. Richter and C.F. Sechrist, Jr., *J. Atmos. Terr. Phys.* **41**, 579 (1979).
12. E.S. Richter, J.R. Rowlett, C.S. Gardner, and C.F. Sechrist, Jr., *J. Atmos. Terr. Phys.* **43**, 327 (1981).
13. C.S. Gardner and D.G. Voelz, *Geophys. Res. Lett.* **12**, 765 (1985).
14. C.S. Gardner, J.L. Bufton, and C.R. Philbrick, in *Digest of Topical Meeting on Optical Remote Sensing of the Atmosphere* (Optical Society of America, Washington, D.C., 1985), Paper WC29.
15. Solid State Research, Lincoln Laboratory, MIT (1987:3), pp. 25 and 26.

3. MATERIALS RESEARCH

3.1 RESIDUAL INFRARED ABSORPTION IN Ti:Al₂O₃ CRYSTALS

The performance of Ti:Al₂O₃ lasers is impaired generally by an infrared absorption that occurs in the laser output wavelength region. On the basis of data for as-grown and annealed samples cut from Ti:Al₂O₃ crystals grown by the vertical-gradient-freeze (VGF) technique, we previously proposed¹ that the residual absorption is due to Ti³⁺ – Ti⁴⁺ pairs. In this report, we present additional data that confirm this ion-pair model for the residual absorption, which can be attributed to excitation of the 3d electron of the Ti³⁺ ion perturbed by the Coulomb field of the neighboring Ti⁴⁺ ion and/or an associated Al vacancy.

We have reported¹ that annealing as-grown VGF Ti:Al₂O₃ crystals at high temperatures ($\approx 1600^\circ\text{C}$) in a reducing atmosphere (an Ar-H₂ mixture) decreases the residual absorption without significantly changing the main absorption due to Ti³⁺ ions, which peaks at about 490 nm, while annealing in an oxidizing atmosphere (an Ar-O₂ mixture) increases the residual absorption and simultaneously decreases the main absorption. The decrease in the main absorption, which also was observed²⁻⁴ in earlier experiments on Ti:Al₂O₃ crystals grown by the Czochralski method, results from the oxidation of Ti³⁺ ions to Ti⁴⁺ ions. It is probable that an Al vacancy is formed for every three Ti³⁺ ions converted into Ti⁴⁺.⁴ The oxidation reaction is reversible, since annealing oxidized samples in a reducing atmosphere restores the main absorption.²⁻⁴

If the residual absorption is due to Ti³⁺ – Ti⁴⁺ pairs, the absorption coefficient α_r at a given wavelength in the residual absorption band will be proportional to the concentration of these pairs and therefore to the product, $[\text{Ti}^{3+}][\text{Ti}^{4+}]$, of the Ti³⁺ and Ti⁴⁺ concentrations. We have established that the absorption coefficient α_m at the peak of the main absorption band in Ti:Al₂O₃ is proportional to $[\text{Ti}^{3+}]$.⁵ If annealing results only in the conversion of Ti³⁺ ions to Ti⁴⁺ ions or vice versa, without changing the total concentration $[\text{Ti}]$ of these ions, then $[\text{Ti}^{4+}] = [\text{Ti}] - [\text{Ti}^{3+}]$. This difference is proportional to $(\alpha_o - \alpha_m)$, where α_o is the value of α_m when all the ions are in the Ti³⁺ state. In this case,

$$\alpha_r = C\alpha_m(\alpha_o - \alpha_m) \quad , \quad (3-1)$$

where C is a constant. According to this expression, $\alpha_r = 0$ when $\alpha_m = 0$ or $\alpha_m = \alpha_o$, i.e., when the Ti ions are either all in the Ti⁴⁺ state or all in the Ti³⁺ state.

From Equation (3-1),

$$\alpha_r/\alpha_m = C\alpha_m(\alpha_o - \alpha_m) \quad , \quad (3-2)$$

Equation (3-2) can be used to determine C and α_o from data for α_r as a function of α_m for samples with constant $[\text{Ti}]$, since a plot of α_r/α_m vs α_m will be a straight line with slope of $-C$ and intercept of α_o on the α_m axis.

Equation (3-1) may be rewritten as

$$\alpha_r = C[(1 - \beta)/\beta]\alpha_m^2, \quad (3-3)$$

where $\beta \equiv \alpha_m/\alpha_0 = [\text{Ti}^{3+}]/[\text{Ti}]$, the fraction of the Ti ions in the Ti^{3+} state. For a series of samples with constant β but different values of $[\text{Ti}]$, according to Equation (3-3), α_r varies quadratically with α_m . For a series of samples with constant $[\text{Ti}]$, the maximum value of α_r is obtained for $\beta = 1/2$, when $[\text{Ti}^{3+}] = [\text{Ti}^{4+}]$:

$$\alpha_r(\text{max}) = (1/4) C\alpha_0^2. \quad (3-4)$$

To test the validity of the $\text{Ti}^{3+} - \text{Ti}^{4+}$ model, we have measured the dependence of α_r on α_m for samples with different values of β but the same value of $[\text{Ti}]$.

The equilibrium oxygen stoichiometry of $\text{Ti:Al}_2\text{O}_3$, and therefore the equilibrium value of β , is determined by the temperature and the O_2 partial pressure in the ambient gas phase. Changes in stoichiometry during annealing take place by the diffusion of crystal defects (probably the Al vacancies) into or out of the solid. Uniform samples with various β values can be obtained by annealing in controlled atmospheres at a temperature where the diffusion rate is high enough for equilibrium with the gas phase to be attained in a practical time (hours or days), then cooling rapidly to quench in the high-temperature stoichiometry. If the annealing time is too short, however, the sample will exhibit a gradient in β in the direction normal to the surface. Figure 3-1 shows the results of measurements on such a nonequilibrium sample, which was obtained fortuitously when an as-grown VGF sample was annealed at 1600°C in an Ar- O_2 atmosphere. As shown schematically in the inset of Figure 3-1, the exterior of the sample was colorless, while the interior retained the characteristic pink color of $\text{Ti:Al}_2\text{O}_3$. The transmission through the long dimension of the sample, which was perpendicular to the c-axis, was measured for a $\text{Ti:Al}_2\text{O}_3$ laser at 780 nm and for an Ar-ion all-line laser, each focused to a spot size about $250 \mu\text{m}$ in diameter. By making measurements in the π polarization at different points along the mid-line of the end face, pairs of α_r and α_m values were determined for different values of β but the same value of $[\text{Ti}]$. These data yield the plot of α_r vs α_m shown in Figure 3-1, which has the parabolic form expected for the $\text{Ti}^{3+} - \text{Ti}^{4+}$ model. The same data have been used to obtain the plot of α_r/α_m vs a_m shown in Figure 3-2. The points fit a straight line, as predicted by Equation (3-2), thus confirming the $\text{Ti}^3 - \text{Ti}^4$ model for the residual absorption.

R.L. Aggarwal	R.E. Fahey
A. Sanchez	A.J. Strauss
M.M. Stuppi	

3.2 Pt-Ir SILICIDE SCHOTTKY-BARRIER IR DETECTORS

To fabricate Schottky-barrier infrared (IR) detectors, a silicide-Si Schottky diode is formed by depositing a noble metal film on a p-type Si substrate, then annealing to convert the metal to the corresponding silicide by reaction with the substrate. Platinum silicide (PtSi) detectors have a barrier height of 0.22 eV and a cutoff wavelength of $\sim 5.6 \mu\text{m}$.⁶ Imager arrays containing more than 250,000 detector elements have been demonstrated.^{7,8}

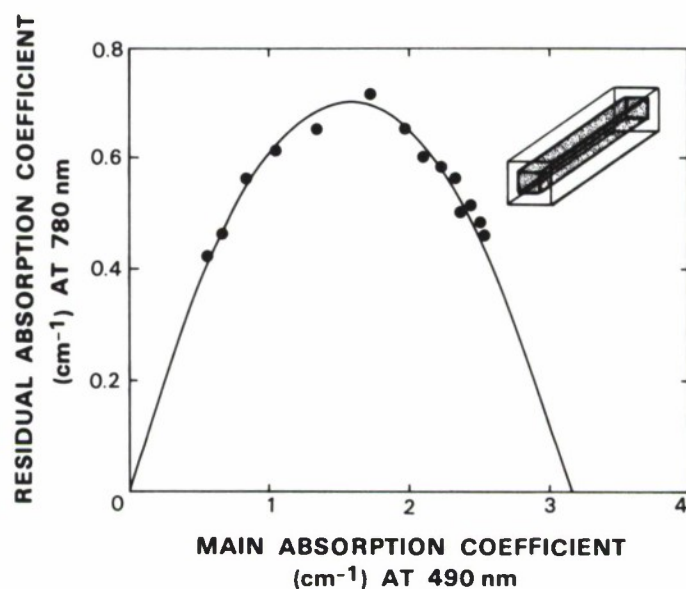


Figure 3-1. Residual absorption coefficient α_r at 780 nm vs main absorption coefficient α_m at 490 nm measured at room temperature in the π polarization for a partially oxidized VGF sample of $\text{Ti:Al}_2\text{O}_3$.

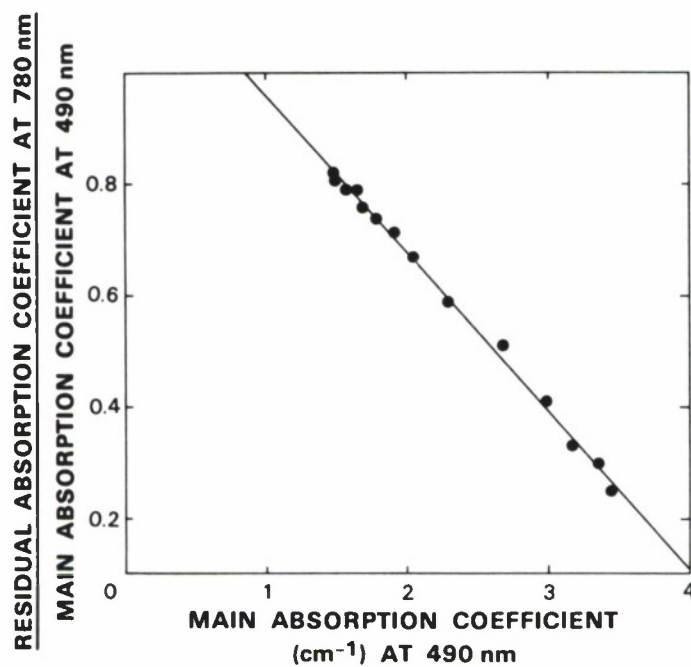


Figure 3-2. Plot of α_r/α_m vs α_m obtained from data of Figure 3-1. Values of C and α_0 determined from the straight line in accordance with Equation (3-2) were used to calculate the parabola shown in Figure 3-1.

There is strong interest in extending the response of Schottky-barrier detectors into the spectral band from 8 to 14 μm . Iridium silicide photodiodes have the potential for achieving such an extended response, since barrier heights of 0.125-0.152 eV, corresponding to cutoff wavelengths of 8-10 μm , have been measured^{9,10} for such devices. However, Ir silicide detectors have poor diode characteristics and low quantum efficiencies, and their characteristics are not reproducible. These properties are explained by the poor quality of the silicide-Si interface, which can be attributed largely to the fact that Si is the dominant diffusing species in the reaction between Ir and Si.¹¹ During this reaction, therefore, native oxide or other contaminants initially present on the substrate surface will remain at or near the interface. Furthermore, Ir tends to react with the native oxide to form Ir oxide, which can form a diffusion barrier that impedes the formation of Ir silicide. In contrast, Pt is the dominant diffusing species in the reaction between Pt and Si.¹²

In this report, we describe the performance of silicide Schottky-barrier detectors formed by successive deposition of Pt and Ir films. These Pt-Ir devices have significantly better diode electrical characteristics and quantum efficiencies than Ir-only control devices, and their cutoff wavelengths reach 9 μm . Furthermore, the properties of the Pt-Ir diodes are uniform from wafer to wafer and reproducible from run to run.

Devices were fabricated on p-type (100) Si wafers with a resistivity of 30 $\Omega\text{ cm}$. Figure 3-3 is a schematic cross-sectional diagram of the device structure, which incorporates a p^+ substrate contact, a silicide electrode, and an n-type guard ring around the periphery of the silicide to suppress edge leakage. The silicide was formed by sequential electron-beam deposition of a Pt film 5-10 \AA thick and an Ir film 10-20 \AA thick, followed by furnace annealing at 400-500°C in N_2 ambient. To prepare control devices, only a single layer of either Pt or Ir, ~ 20 \AA thick, was used.

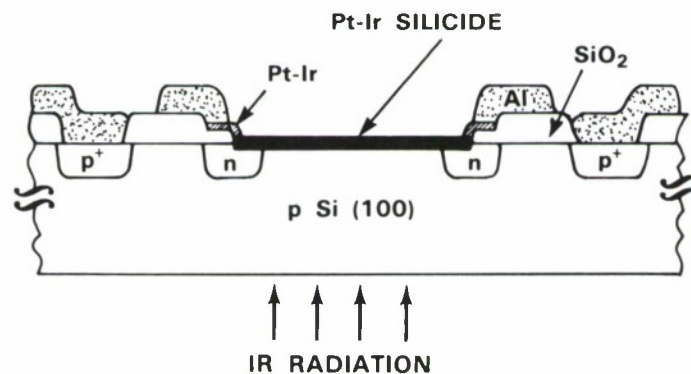


Figure 3-3. Schematic structure of silicide Schottky-barrier infrared detector with Pt-Ir silicide electrode.

The devices were mounted in black ceramic packages with a throughhole to expose the Si substrate for optical characterization. Figures 3-4(a) and 3-4(b) show forward and reverse diode characteristics measured at 77 K for Pt, Ir, and two Pt-Ir devices. The total thickness of metal deposited, ~ 20 \AA , was approximately the same for all devices. The Pt and Pt-Ir devices have

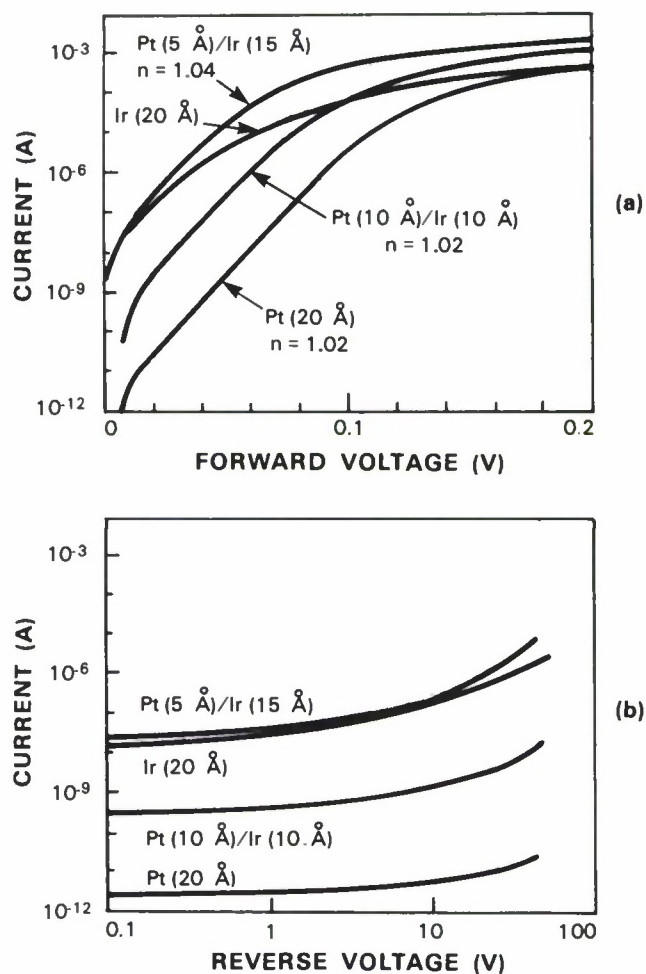


Figure 3-4. (a) Forward and (b) reverse current-voltage characteristics at 77 K for Pt, Ir, and Pt-Ir silicide Schottky-barrier diodes.

good forward characteristics with near-unity ideality factors, while the Ir device has a high, ill-defined ideality factor and high series resistance. All four devices show good reverse characteristics with breakdown voltages exceeding 50 V, but, with increasing reverse bias, the leakage current increases more rapidly for the Ir device than for the others. The Schottky barrier heights deduced from the diode saturation current densities at 77 K are 0.220, 0.188, 0.163, and 0.160 eV for the Pt, Pt(10 Å)/Ir(10 Å), Ir, and Pt(5 Å)/Ir(15 Å) devices, respectively.

The detection of radiation by silicide Schottky-barrier devices takes place by the process of internal photoemission. Photons incident on the Si substrate are transmitted through the Si and absorbed in the silicide, where they produce electron-hole pairs. A photocurrent is generated because a certain fraction of the holes with energies exceeding the barrier height at the silicide-Si

interface are emitted into the Si. The detector responsivity R is generally given to a good approximation by¹³

$$R = C_1 \left(1 - \frac{\lambda\psi}{1.24} \right)^2, \quad (3-5)$$

where C_1 is the emission coefficient (in eV^{-1}), ψ is the barrier height (in eV), and λ is the wavelength (in μm).

For the devices of Figure 3-4, we have measured R at a series of reverse bias voltages between 0 and 50 V over the wavelength range from 1.3 to $6.0 \mu\text{m}$. Both R and the cutoff wavelength increased slightly with increasing bias. In Figure 3-5, the values of R measured at a reverse bias voltage of 50 V are plotted against λ for the Pt, Ir, and Pt(5 Å)/Ir(15 Å) devices. The solid curves in Figure 3-5 were calculated from Equation (3-5) by adjusting the values of C_1 and ψ to give the best fit to the data for the longer wavelengths. For the Pt device, $C_1 = 0.23 \text{ eV}^{-1}$ and the cutoff wavelength $\lambda_c \equiv 1.24/\psi$ is $5.9 \mu\text{m}$. The high C_1 value indicates that both the PtSi layer and the PtSi-Si interface are of excellent quality. For the Ir device, the C_1 value is reduced by a factor of almost 8, but λ_c is increased to $8.4 \mu\text{m}$. For the Pt-Ir device, λ_c is further increased to $9.2 \mu\text{m}$, and C_1 is about three times larger than the value for the Ir device.

The experimental data of Figures 3-4 and 3-5 show that deposition of an extremely thin Pt layer before deposition of Ir yields Schottky-barrier detectors with much better electrical

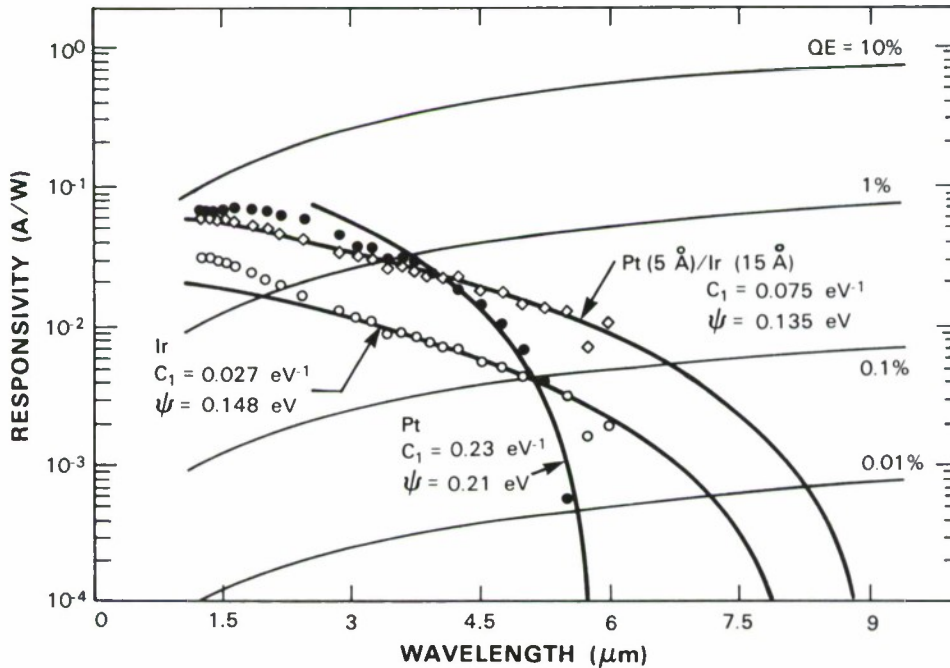


Figure 3-5. Responsivity as a function of wavelength for Pt, Ir, and Pt-Ir silicide Schottky-barrier detectors.

characteristics and quantum efficiencies than those of the control Ir devices. These changes can be attributed to improvements in the material quality of both the silicide-Si interface and the silicide film that occur because the Pt layer reduces the effect of native oxides and other contaminants initially present on the Si surface. The value of ψ for our control Ir detectors is somewhat higher than the lowest reported values,^{9,10} probably because the material quality of these detectors is not as good as the best obtained previously. For the Pt(5 Å)/Ir(15 Å) detectors, ψ is slightly smaller than the value for the control Ir devices. For the Pt(10 Å)/Ir(10 Å) detectors, ψ is somewhat larger than the value for the control Ir devices, but remains well below the value for the control Pt devices. It appears that the improvement in material quality obtained by using Pt tends to decrease ψ , while incorporation of Pt in the silicide film tends to increase ψ .

B-Y. Tsaur

REFERENCES

1. R.E. Fahey, A.J. Strauss, A. Sanchez, and R.L. Aggarwal, in *Tunable Solid State Lasers II*, Springer Series in Optical Sciences, Vol. 52, edited by A.B. Budgor, L. Esterowitz, and L.G. DeShazer (Springer-Verlag, New York, 1987), pp. 82-88.
2. G.A. Keig, *J. Cryst. Growth* **2**, 356 (1968).
3. T.P. Jones, R.L. Coble, and C.J. Mogab, *J. Am. Ceram. Soc.* **52**, 331 (1969).
4. S.K. Mohapatra and F.A. Kröger, *J. Am. Ceram. Soc.* **60**, 381 (1977).
5. R.L. Aggarwal, A. Sanchez, R.E. Fahey, and A.J. Strauss, *Appl. Phys. Lett.* **48**, 1345 (1986).
6. B.R. Capone, L.H. Skolnik, R.W. Taylor, F.D. Shepherd, S.A. Roosild, W. Ewing, W.F. Kosonocky, and E.S. Kohn, 22nd International Technical Symposium, SPIE, San Diego, California, August 1978.
7. W.F. Kosonocky, F.V. Shallcross, T.S. Villani, and J.V. Groppe, *IEEE Trans. Electron Devices* **ED-22**, 1564 (1985).
8. M. Kimata, M. Denda, N. Yutani, S. Iwade, and N. Tsabouchi, *IEEE ISSCC Digest of Technical Papers* (1987), pp. 110-111.
9. P.W. Pellegrini, A. Golubovic, C.E. Ludington, and M.M. Weeks, *IEDM Tech. Dig.* (1982), pp. 157-160.
10. P.W. Pellegrini, A. Golubovic, and C.E. Ludington, *SPIE Symposium*, New Orleans, Louisiana, May 1987.
11. S. Petersson, J. Baglin, W. Hammer, F. D'Heurle, T.S. Kuan, I. Ohdomari, J. de Sousa Pives, and P. Tove, *J. Appl. Phys.* **50**, 3357 (1979).
12. K.N. Tu, *Appl. Phys. Lett.* **27**, 221 (1975).
13. V.L. Dalal, *J. Appl. Phys.* **42**, 2274 (1971)

4. MICROELECTRONICS

4.1 NEW MBE BUFFER FOR MICRON- AND QUARTER-MICRON-GATE GaAs MESFETs

A new buffer layer has been developed that eliminates backgating in GaAs MESFETs and substantially reduces short-channel effects in GaAs MESFETs with 0.27- μm -long gates. The new buffer is grown by molecular beam epitaxy (MBE) at a substrate temperature of 200°C using Ga and As₄ beam fluxes. The buffer is crystalline, highly resistive, optically inactive, and can be overgrown with high quality GaAs. GaAs MESFETs with a gate length of 0.27 μm that incorporate the new buffer show improved dc and RF properties in comparison with a similar MESFET with a thin undoped GaAs buffer.

To demonstrate the backgating performance improvement afforded by the new buffer, MESFETs were fabricated using a number of different buffer layers and structures.¹ A schematic cross section of the MESFET structure used in this study is shown in Figure 4-1. The measured gate length, gate width, and source-drain spacing of this device are 2, 98, and 5.5 μm , respectively. An ohmic contact, isolated from the MESFET by mesa etching, served as the

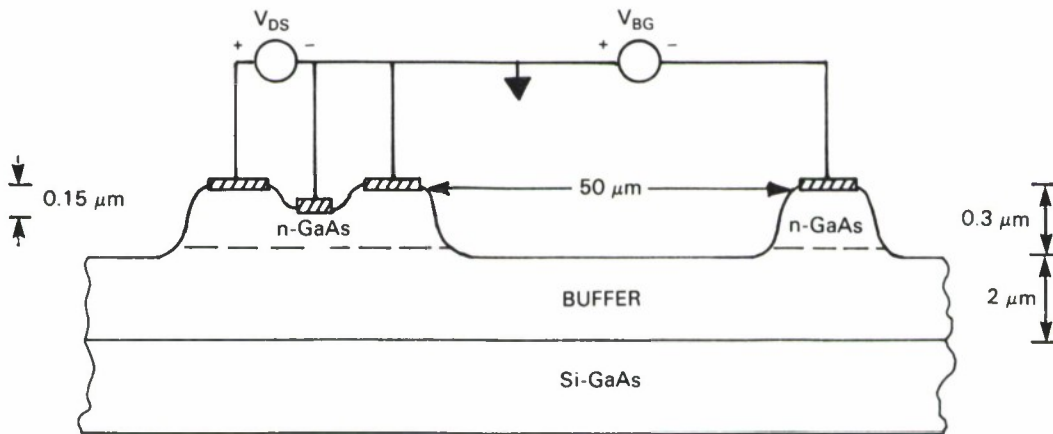


Figure 4-1. Schematic cross section of the MESFET structure used to measure backgating.

sidegate. The MESFETs were fabricated in MBE n-GaAs layers grown upon the new buffer and also in MBE n-GaAs layers grown upon buffer layers of undoped GaAs, AlGaAs, and GaAs/AlGaAs superlattices. All the buffer layers were grown by MBE and are 2 μm thick. The active layer is doped to approximately $2 \times 10^{17} \text{ cm}^{-3}$ with silicon and is 0.3 μm thick. MESFETs also were fabricated in commercial vapor phase epitaxy n-GaAs layers deposited on semi-insulating (SI) GaAs substrates and on layers made by direct ion implantation into the SI GaAs substrates. The gate recess depth is roughly half the active layer thickness, and mesa etching was used to isolate the devices. The ohmic contacts are alloyed Ni (or Pd)/Ge/Au, and the Schottky contact is Ti/Au.

The most dramatic improvement in device performance provided by the new buffer is the elimination of backgating, as illustrated by Figure 4-2.¹ The normalized I_{DSS} is plotted versus the applied backgating voltage V_{BG} . A sidegate spaced 50 μm from the MESFET and $V_{DS} = 2.5\text{ V}$ are used. Data obtained both in the dark and in white light are shown. The lines in the figure are included only as a convenience in visualizing the data.

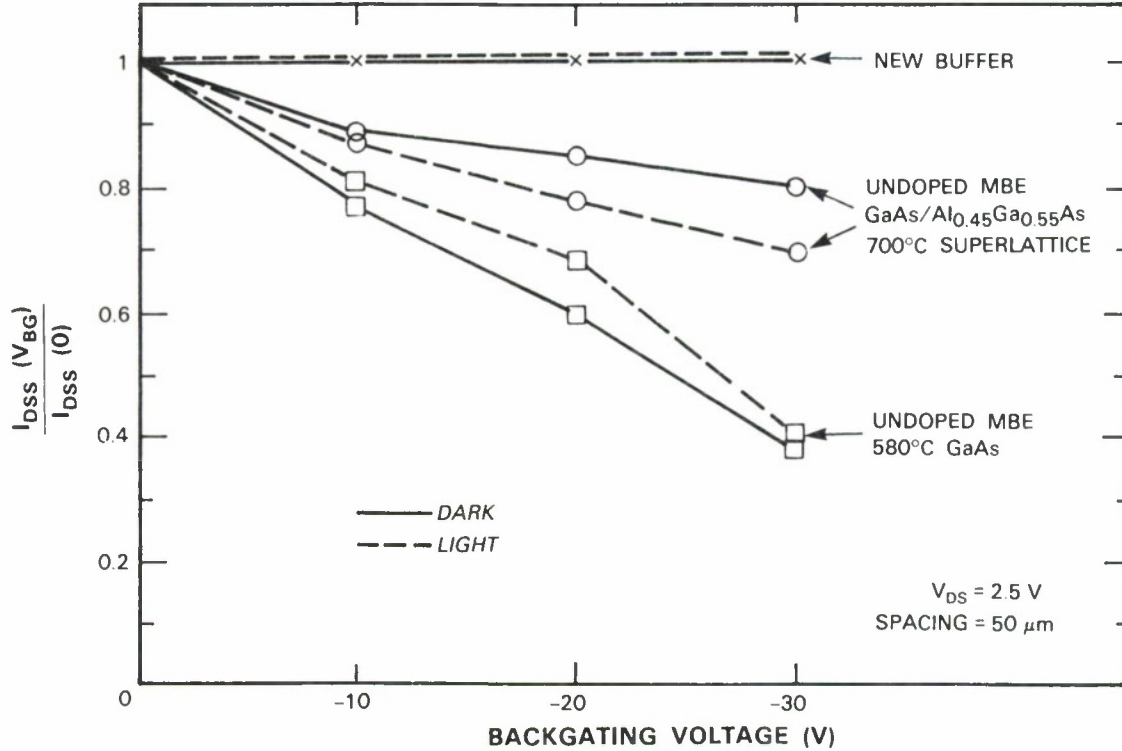


Figure 4-2. Backgating characteristics: new MBE buffer, undoped GaAs buffer, and undoped superlattice buffer. The solid lines indicate the results obtained in the dark and the dashed lines in the light.

Figure 4-2 compares backgating MESFETs fabricated in active layers on the new buffer with backgating in MESFETs fabricated in active layers on an undoped GaAs buffer and on an undoped GaAs/ $\text{Al}_{0.45}\text{Ga}_{0.55}\text{As}$ superlattice buffer grown by MBE at 700°C. Both GaAs- and superlattice-buffered devices show backgating and light sensitivity, while the device with the new buffer shows neither. Although not shown here, MESFETs fabricated using all of the other buffers show light sensitivity and backgating. Of the alternative buffers, the AlGaAs and superlattice buffers grown at 700°C appear to be the best.

Although the data presented in Figure 4-2 were obtained using a sidegate spaced 50 μm from the MESFET, a sidegate spaced 15 μm from the MESFET also was used. For -50 V applied to this sidegate and $V_{DS} = 2.5\text{ V}$, the new buffered device still showed no backgating.

For the same voltage, I_{dss} of the superlattice-buffered MESFET was reduced by 50% and the GaAs-buffered devices destructively broke down.

Several of the short-channel effects noted in the introduction were reduced substantially by using the new buffer in a 0.27- μm -gate-length MESFET. Figure 4-3 shows a top view of the MESFET used in this study. Figure 4-3(a) is an SEM photograph of the entire device and Figure 4-3(b) is a magnified view of the gate region. The MESFET has multiple gate connections to minimize gate resistance, and the segmented source is connected by air bridges. The gate was defined in a single layer of PMMA using electron beam lithography. The measured gate length, gate width, and source-drain spacing are 0.27, 200 and 2 μm , respectively. All of the following dc and RF measurements were made on this device.

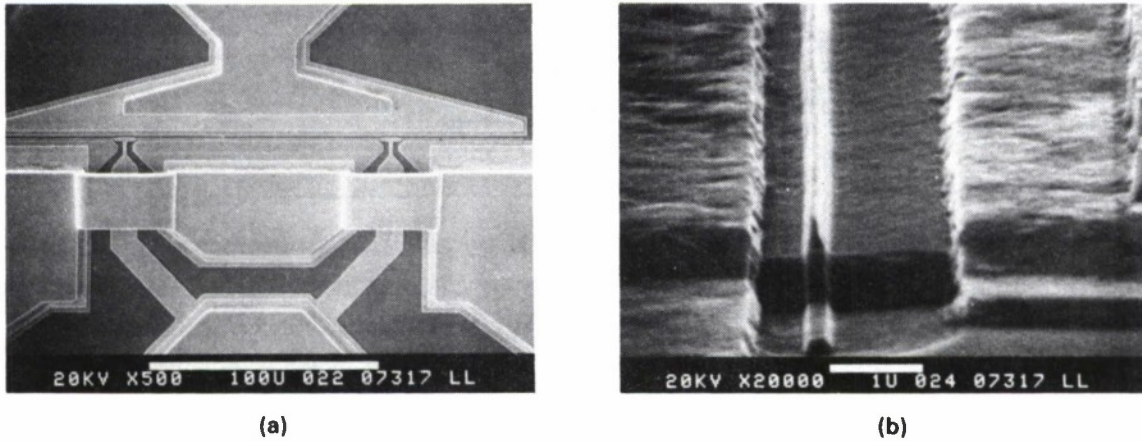


Figure 4-3. SEM photographs of the 0.27- μm MESFET: (a) top view of the device, and (b) magnified view of the gate region.

In Figure 4-4 are shown schematic cross sections of 0.27- μm MESFETs made with the new buffer and also with an undoped GaAs buffer. The starting material is SI GaAs and all epitaxial layers were deposited by MBE. The device with the undoped GaAs buffer has a 3300- \AA -thick buffer layer, a 1200- \AA -thick active layer doped to $6 \times 10^{17} \text{ cm}^{-3}$ with silicon, and a thin heavily doped n^+ GaAs cap layer doped to $2 \times 10^{18} \text{ cm}^{-3}$ with silicon. The device with the new buffer layer has a 1- μm -thick buffer, a 100- \AA -thick undoped GaAs region that has a planar (impulse) doping of silicon halfway through it, a 1200- \AA -thick active layer doped to $6 \times 10^{17} \text{ cm}^{-3}$ with silicon, and a thin n^+ cap. The silicon planar doping of $4.8 \times 10^{12} \text{ cm}^{-2}$ is included in the device with the new buffer to increase the transconductance g_m near pinch-off. The gates are recessed to a depth that yields the same drain-source current for both devices, and mesa etching is used for device isolation. The ohmic contacts are alloyed Ni/Ge/Au and the Schottky contact is Ti/Au.

Improved RF performance of the 0.27- μm MESFET incorporating the new buffer also has been observed. The maximum frequency of oscillation (f_{max}) and unity current gain frequency (f_T) have been calculated from the measured scattering parameters and are shown in Table 4-1.

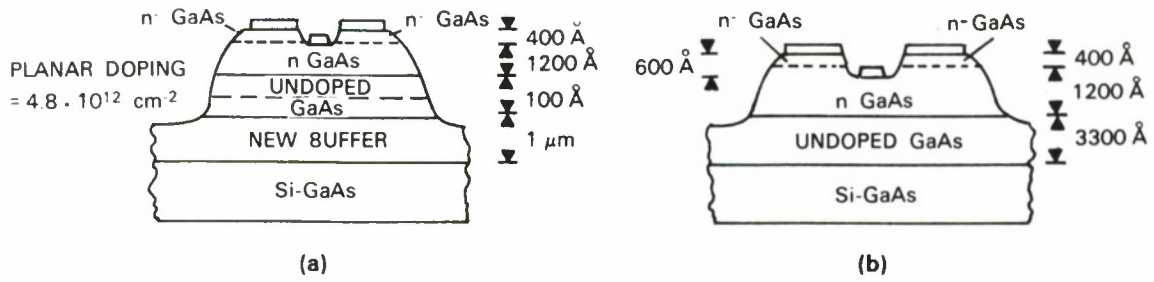


Figure 4-4. Schematic cross sections of the 0.27- μm MESFETs: (a) new MBE buffer, and (b) undoped GaAs buffer.

<p>TABLE 4-1</p> <p>Summary of RF Results</p> <p>0.25-μm MESFETs</p>			
Properties		Undoped MBE GaAs Buffer	New MBE Buffer
Maximum Stable Gain at 26 GHz	(dB)	10.4	12.0
f_T	(GHz)	26	28
f_{max}	(GHz)	80	91

The maximum stable gain (MSG) at 26 GHz for the new MBE buffered device is 12 dB, and f_{max} and f_T are 91 and 28 GHz, respectively, for the new MBE buffered device. These results were measured for $V_{\text{ds}} = 2$ V and did not change appreciably for V_{ds} up to 6 V. These values of MSG, f_{max} , and f_T for the MESFETs using the new buffer are significantly better than those measured on comparable MESFETs using an undoped MBE GaAs buffer and are among the best we have measured for MESFETs fabricated by the same process with a gate length of 0.27 μm .

F.W. Smith L.J. Mahoney
A.R. Calawa M.J. Manfra
C.L. Chen

4.2 ADVANCED DEVICE FABRICATION WITH ANGLED CHLORINE ION-BEAM-ASSISTED ETCHING

Angled ion-beam-assisted etching (IBAE) has been used in conjunction with a variety of lithographic techniques to produce structures in GaAs and GaAlAs with controlled sidewall geometries. We currently are utilizing this technology to fabricate vertical FETs, resonant tunneling transistors, surface emitting laser arrays and quantum-wire structures.

The basic chlorine IBAE and angled chlorine IBAE processes and equipment have been described elsewhere.²⁻⁴ For this work, we adjusted the system operating parameters to give a normal-incident etch rate of 40 to 50 nm min⁻¹ in GaAs. We operated the system with a 500-eV argon ion beam at a current density of 0.02 mA cm⁻², which gave an argon ion beam pressure of 0.1 mTorr at the sample surface. The chlorine beam pressure at the sample surface was 2.8 mTorr. With these parameters, the normal-incidence etch rates for Al_xGa_{1-x}As with x from 0.08 to 0.80 were 40 nm min⁻¹ to within 10%. No roughness was observed at GaAs-AlGaAs heterointerfaces. The masking materials were baked AZ-1470 photoresist, pyrolytically deposited phosphosilicate glass and evaporated nickel. The respective etch rates for these materials were 4.7 nm min⁻¹, 1.2 nm min⁻¹, and 0.4 nm min⁻¹.

The technique was used to fabricate a monolithic two-dimensional GaAs/AlGaAs laser diode array with light emission normal to the surface. This was accomplished by fabricating an array of edge-emitting quantum-well double-heterostructure lasers with deflecting mirrors adjacent to the laser facets.⁵ A laser array is shown schematically in Figure 4-5(a). The first step in the fabrication of the array was to etch the laser facets. With photoresist as an etch mask, chlorine IBAE was used to etch pairs of straight-sided grooves which were 2 μm wide and about 3 μm deep and were parallel to the (011) cleavage plane. The outer facets of each pair of grooves act as the mirrors for the rows of laser cavities, which are 250 μm long. Lines about 3 μm wide immediately adjacent to the inside edge of one of the etched grooves in each pair then were opened in a new layer of photoresist, and parabolic deflectors for one side of each laser row were formed by continuously varying the tilt angle during etching to form deflectors. The deflector mirror for the other side of each laser row was then formed in a similar manner. Further details of the processing are contained in Reference 4.

Arrays consisting of 20-30 laser elements were cleaved from the wafer, mounted for testing and evaluated during pulsed (100-ns pulses, 1-kHz repetition rate) operation. Figure 4-5(b) shows the near-field pattern of a 22-element array consisting of two rows of 11 laser elements bonded in parallel. The middle spots are actually a combination of the outputs from one end of a laser in each row and therefore appear larger than the outside spots. The threshold current for the entire array was about 3.5 A, corresponding to an average threshold current for each laser element of about 160 mA. The differential quantum efficiency was about 15%. The peak output power was 1.6 W at 10.5 A.

The fabrication of ultrasmall GaAs-based structures has progressed rapidly in the past several years. We have used masked ion beam lithography (MIBL) in combination with angled chlorine IBAE to produce structures in GaAs with dimensions less than 10 nm.^{6,7} In our

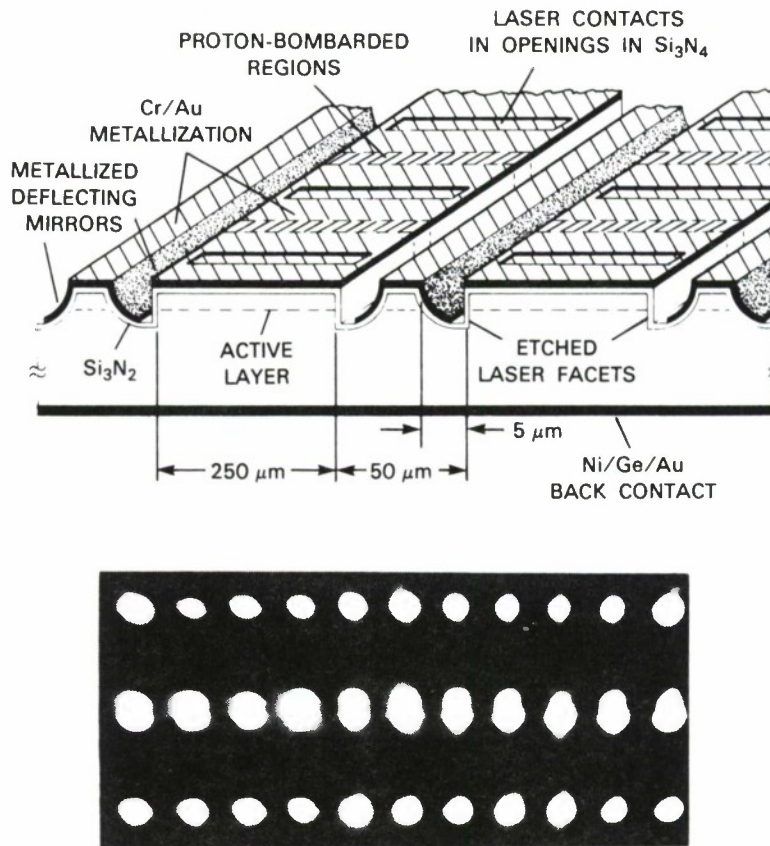


Figure 4-5. (a) Schematic diagram of a monolithic surface-emitting two-dimensional GaAs/AlGaAs laser diode array, and (b) near-field pattern of a typical array.

approach to fabricating such structures, MIBL is first used to pattern submicrometer features in a PMMA layer that has been spun on a GaAs substrate, and metal evaporation and lift-off is used to transfer the developed PMMA patterns to a metal etch mask. An initial chlorine IBAE etching step then is performed, creating features such as columns in the substrate, the metal mask is removed, and the columns are thinned with angled chlorine IBAE. To demonstrate the technique, we have patterned a Ni etch mask consisting of 80-nm-wide by 1.8-μm-long rectangular boxes on a GaAs substrate, etched the substrate approximately 0.5 μm deep to form columns, removed the mask, and then thinned the columns to widths of less than 10 nm. Figure 4-6 is a schematic diagram that illustrates the thinning process. The technique etches smooth facets in layered GaAs, AlAs, and AlGaAs structures without modification and is therefore useful for fabricating quantum wires and boxes from GaAs/AlGaAs quantum-well layers for optical studies.

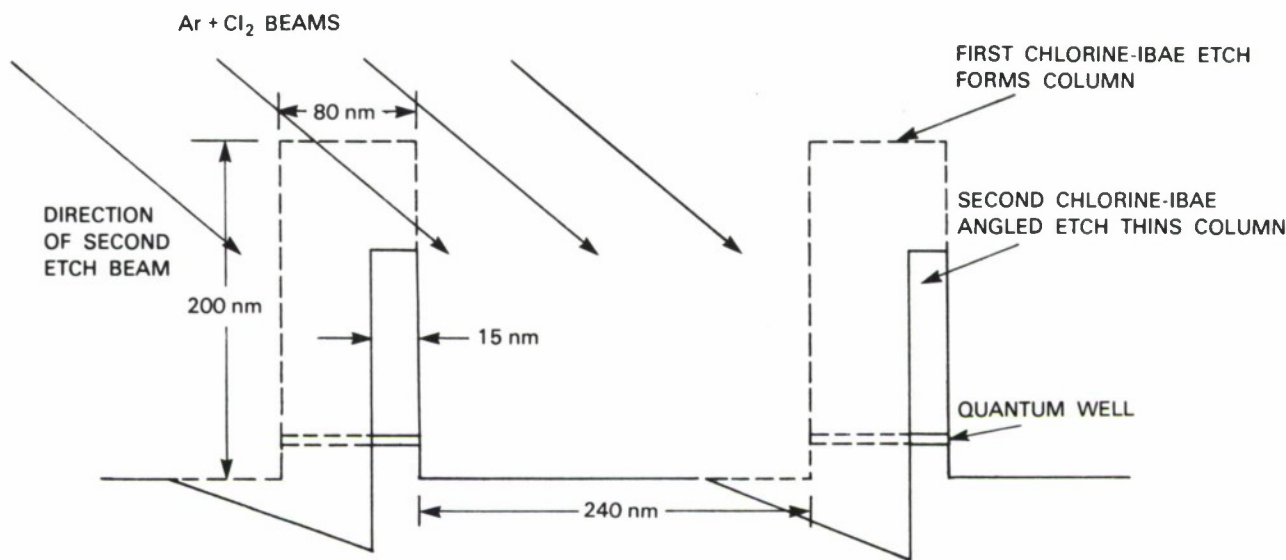


Figure 4-6. Schematic diagram illustrating the two-step process for fabricating nanometer-size structures such as quantum wires. After the initial etch, the masking layer is removed and a second angled etch is used to thin the columns.

Figure 4-7 shows SEM micrographs of the structures produced in GaAs with the technique. Micrograph (a) shows the 80-nm-wide structures resulting from the initial normal-incident chlorine IBAE etch, while micrographs (b), (c), and (d) show the results of angle etching the columns shown in micrograph (a) for 1.0, 1.5, and 2.0 min. The resulting columns have widths of 40, 22, and 9 nm, respectively. As shown in the micrographs, the sidewalls of the columns are fairly smooth. The columns of micrograph (d) are so thin that some of the electrons of the SEM pass through them to image the substrate on the opposite side, giving the columns a ghostly appearance.

A high speed resonant tunneling transistor has been proposed by Sollner *et al.*⁸ The transistor consists of a double-barrier GaAs/AlGaAs resonant tunneling structure with ohmic contacts on both sides of the structure and an ohmic or Schottky barrier contact to the 4-nm-thick resonant well for controlling the current through the device. The major problem in the design of the transistor is making contact to the 4-nm-thick well. Angled chlorine IBAE in combination with molecular beam epitaxy (MBE) might facilitate the fabrication of such a transistor. Figure 4-8 shows a scheme for making such a device. As shown in the figure, angled chlorine IBAE would be used to form a set of fingers with an angled wall slope. After the fingers are defined, MBE would be used to grow a resonant tunneling structure over them. Depending on the sidewall angle and crystallographic direction, a double-barrier resonant tunneling structure would be grown over the fingers, with the thin barriers and well for the device placed on the sidewall and thicker barriers and well for the contact placed on the horizontal surfaces. The

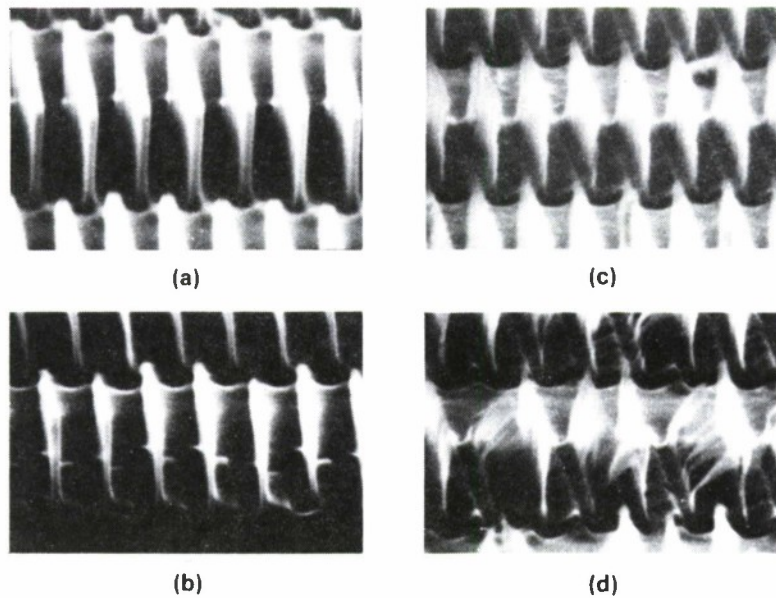


Figure 4-7. SEM micrographs showing (a) 80-nm-wide columns resulting from a normal-incident chlorine IBAE etch, and (b), (c), and (d) the results of angle etching the 80-nm-wide columns of micrograph (a). The columns in micrographs (b), (c), and (d) were etched for 1.0, 1.5, and 2.0 min, respectively, and have respective widths of 40, 22, and 9 nm.

92044-33

angle of the sidewall would be selected to enhance the growth rate difference between the horizontal and sidewall surfaces and ensure the ability of MBE to incorporate Si with low donor compensation on both growing surfaces.^{9,10} We, as well as others, have been able to grow quantum wells with MBE that follow the surface morphology of wet-etched channels.^{11,12} Since chlorine IBAE is primarily a chemical process with much less surface damage than reactive ion etching, we have been able to grow over planar etched surfaces with MBE after a minor cleanup step. Figure 4-9 shows a sketch of a finger-type resonant tunneling structure along with several SEM micrographs of an etched set of fingers.

The angled chlorine IBAE technique also lends itself to the fabrication of vertical FETs. Although several groups have attempted vertical FETs in the past, the angle chlorine IBAE technique has not been employed.^{13,15} Figure 4-10 shows a sketch in cross section of such a transistor. The contact techniques are similar to those of the resonant tunneling transistor. The trimming of the device to adjust the pinch-off voltage is performed by an angled etch that recesses the gate.

The above examples demonstrate the versatility of angled chlorine IBAE as an advanced device fabrication method in the GaAs/AlGaAs materials system. The ability to control the

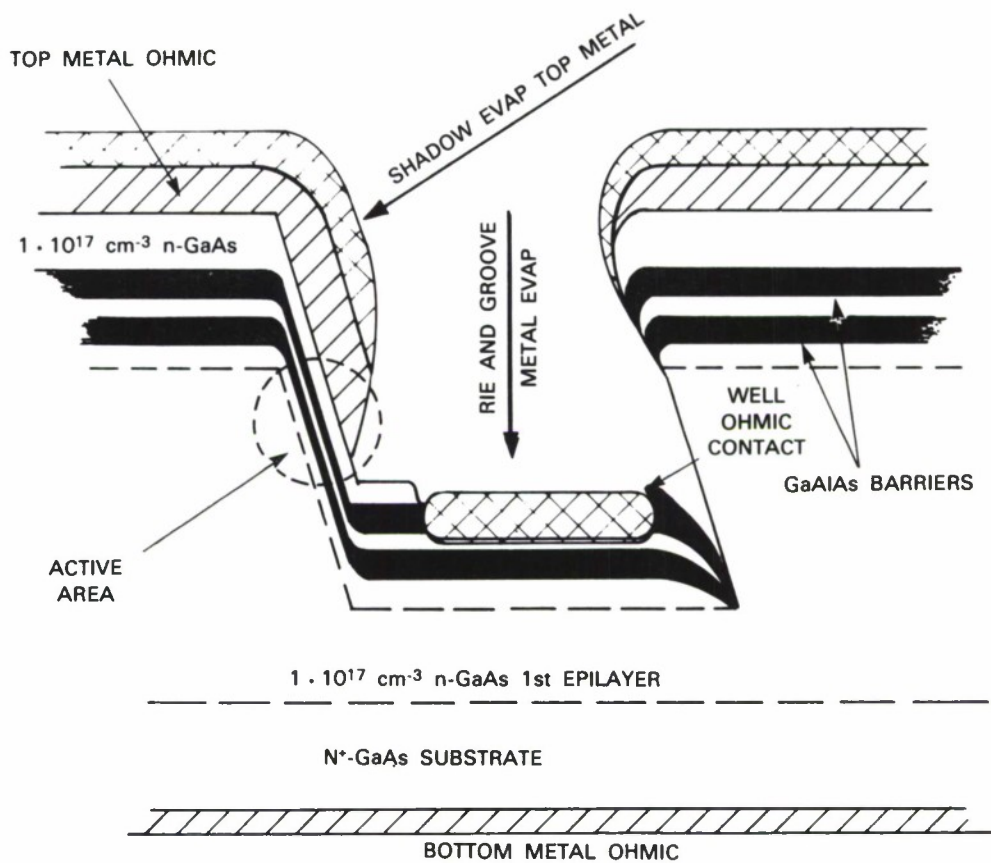


Figure 4-8. Schematic diagram showing a scheme for contacting the quantum well of a resonant tunneling transistor. The key fabrication steps include an angle etch, MBE overgrowth, top contact shadow evaporation, reactive ion etching or second chlorine IBAE to open the well contact, and well contact evaporation.

direction of etching in this materials system provides another parameter that can be used to optimize device performance. The technique is relatively straightforward to implement and the equipment can be constructed from off-the-shelf items.

W.D. Goodhue	M.A. Hollis
S.W. Pang	J.P. Donnelly

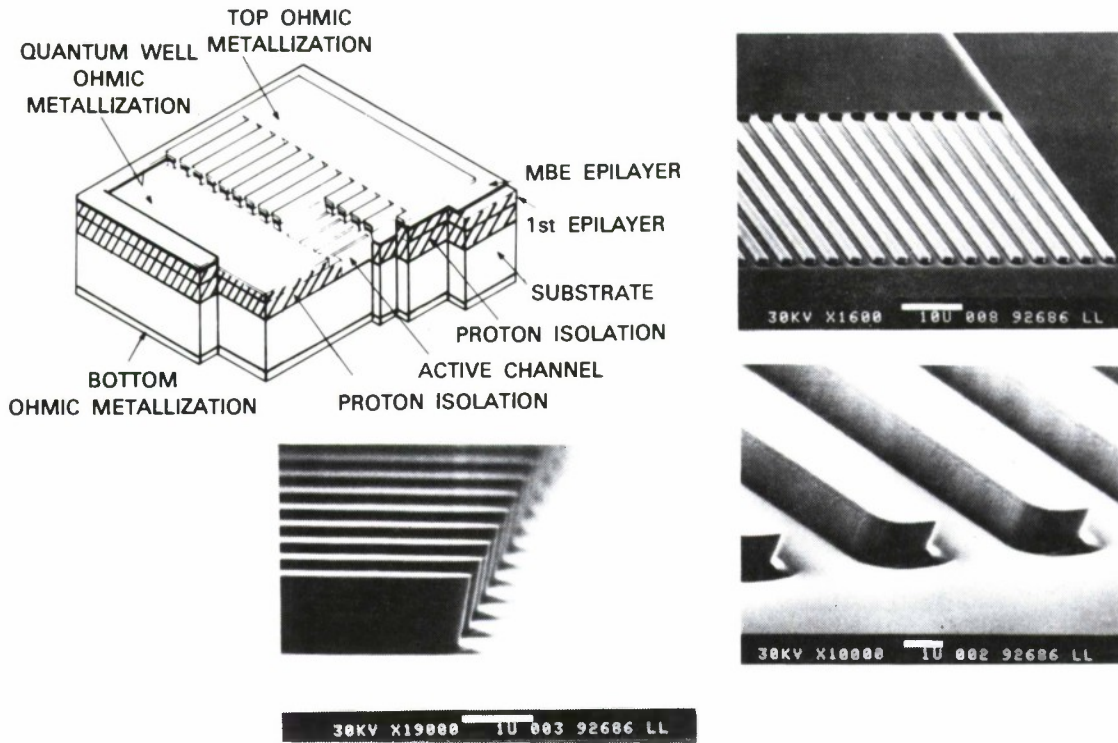


Figure 4-9. Schematic diagram of the proposed resonant tunneling transistor with SEM micrographs showing the finger structure after angled chlorine IBAE. As shown in the micrographs, a compound angle cut was used also to aid in contact isolation.

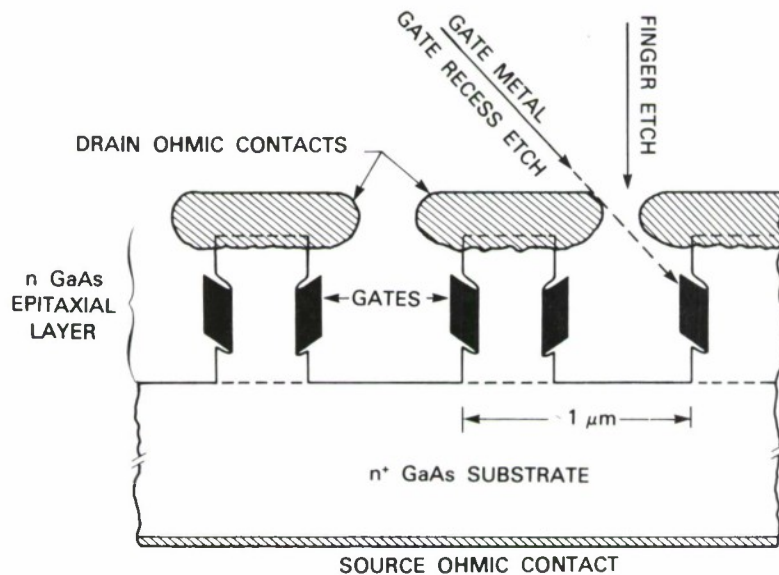


Figure 4-10. Schematic diagram of the proposed vertical FET. In this device, the pinch-off voltage is adjusted with angled etching before the gates are applied.

4.3 SWITCHED-CAPACITOR FILTERS

The most recent design of the SAW/FET wideband programmable transversal filter, described in detail in previous reports,¹⁶⁻¹⁸ incorporates switched-capacitor lowpass filters at each tap to reduce undesirable intermodulation products associated with the programming waveform update rate.

A schematic diagram of a switched-capacitor filter (SCF) is shown in Figure 4-11(a). If the switch is toggled at a frequency of f_c , then the switch and C_1 will approximate a series resistor with a resistance value of $(C_1 f_c)^{-1}$, and the filter will have a cutoff frequency of $C_1 f_c / 2\pi C_2$. The switch can be realized as shown in Figure 4-11(b) by two MOSFET transfer gates driven by nonoverlapping clocks ϕ_1 and ϕ_2 .

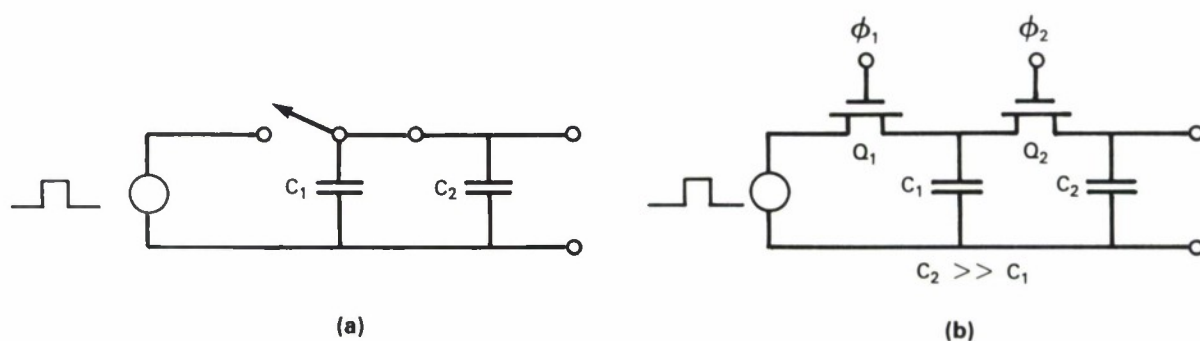
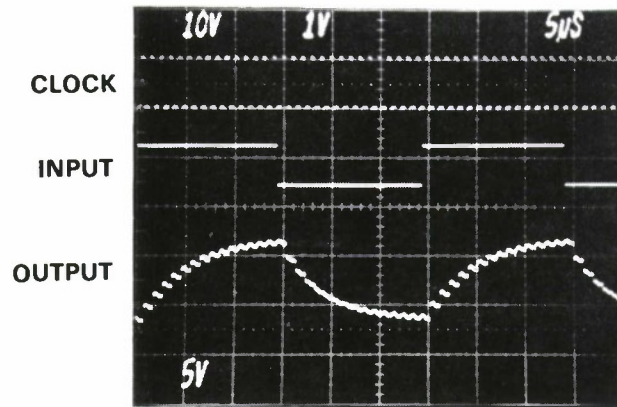


Figure 4-11. Switched-capacitor lowpass filter. (a) Conceptual representation. (b) Realization with MOSFET transfer gates controlled by nonoverlapping clocks.

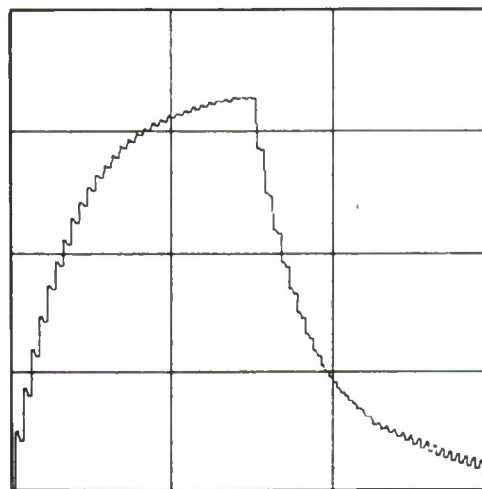
A test structure for this filter was included on each FET chip. The response of one of these structures is shown in Figure 4-12 along with the result of SPICE simulations performed while designing the chip. The measured response is in qualitative agreement with the simulation, although the input amplitude and frequency were not the same for the simulation as for the measured response. The clock feedthrough seen on both the simulated and the measured waveforms is caused by charge stored on the gate of Q_2 and can be reduced by making C_1 and C_2 larger, by reducing the gate area of Q_2 , or by a combination of the two.

Testing of a SAW/FET with an SCF integrated with each of the 700 sense fingers has shown a 3-dB reduction in spurious intermodulation products. Some additional improvement in performance may be obtained by optimizing the SCF characteristics through refinement of the switching rate, duty cycle and capacitance ratio.

D.L. Smythe
V.S. Dolat



(a) MEASURED RESPONSE



(b) SPICE SIMULATION

Figure 4-12. Step response of the switched-capacitor filter at a clock frequency of 1 MHz. (a) Measured response at an update rate of 15 μ s. (b) Calculated response at an update rate of 30 μ s.

REFERENCES

1. F.W. Smith, A.R. Calawa, C.L. Chen, M.J. Manfra, and L.J. Mahoney, submitted to IEEE Electron Device Lett.
2. M.W. Geis, G.A. Lincoln, and W.J. Piacentini, J. Vac. Sci. Technol. **19**, 1390 (1981).
3. G.A. Lincoln, M.W. Geis, S.W. Pang, and N.N. Efremow, J. Vac. Sci. Technol. B **1**, 1043 (1983).
4. W.D. Goodhue, G.D. Johnson, and T.H. Windhorn, in *Gallium Arsenide and Related Compounds 1986* (Inst. Phys. Conf. Ser. 83, Bristol, England, 1987), p. 349.
5. J.P. Donnelly, W.D. Goodhue, T.H. Windhorn, R.J. Bailey, and S.A. Lambert, submitted to Appl. Phys. Lett.
6. J.N. Randall, D.C. Flanders, N.P. Economou, J.P. Donnelly, and E.I. Bromley, J. Vac. Sci. Technol. B **3**, 58 (1985).
7. W.D. Goodhue, S.W. Pang, G.D. Johnson, D.K. Astolfi, and D.J. Ehrlich, submitted to Appl. Phys. Lett.
8. T.C.L.G. Sollner, H.Q. Le, C.A. Correa, and W.D. Goodhue *Proc. IEEE/Cornell Conf. Advanced Concepts High Speed Semicond. Devices and Circuits* (IEEE, New York, 1985), p. 252.
9. D.L. Miller, Appl. Phys. Lett. **47**, 1309 (1985).
10. W.I. Wang, E.E. Mendez, T.S. Kuan, and L. Esaki, Appl. Phys. Lett. **47**, 826 (1985).
11. M. Manno, T. Yuasa, S. Naritsuka, K. Shinozaki, and M. Ishii, Appl. Phys. Lett. **47**, 728 (1985).
12. E. Kapon, M.D. Tamargo, and D.M. Hwang, Appl. Phys. Lett. **50**, 347 (1987).
13. U. Mishra, E. Kohn, and L.F. Eastman, in *International Electron Device Meeting Technical Dig.*, p. 594 (1982).
14. R.C. Clark, H.C. Nathanson, J.G. Oakes, and G.T. Hardison, IEEE Trans. Electron Devices **ED-29**, 1709 (1982).
15. W.R. Frensley, B. Bayraktaroglu, S.E. Campbell, H. Shih, and R.E. Lehmann, IEEE Trans. Electron Devices **ED-32**, 952 (1985).
16. Solid State Research, Lincoln Laboratory, MIT (1986:1), p. 47, DTIC AD-A176097.
17. Solid State Research, Lincoln Laboratory, MIT (1986:4), p. 53, DTIC AD-A182215.
18. Solid State Research, Lincoln Laboratory, MIT (1987:3), pp. 63-65.

5. ANALOG DEVICE TECHNOLOGY

5.1 RF SURFACE RESISTANCE OF $\text{YBa}_2\text{Cu}_3\text{O}_{7-x}$ THIN FILMS

The excitement engendered by the discovery of the new high T_c oxide superconductors¹ has led to much speculation about practical applications of thin films of these materials in digital and analog electronic devices.² Most of these envisioned applications involve high frequency signals for which a detailed knowledge of the surface impedance of the novel superconductors is very important.

We have measured the surface resistance of thin films of YBaCuO in the frequency range $0.5 < f < 17$ GHz using a stripline-resonator method. The stripline procedure also was used to measure the surface resistance of high quality gold and aluminum films; the resistance values obtained agree with values predicted from the measured dc resistance using the Pippard³ formalism for the anomalous skin effect.

The YBaCuO films were produced by a multilayer deposition process. The deposition method has been described in detail elsewhere⁴ and we only present here a cursory description of it. The films are formed by e-beam evaporation of 24 layers of Y, Ba, and Cu. Films with the highest transition temperature were obtained using yttria-stabilized zirconia (YSZ) substrates. The relevant parameters for these films are shown in Table 5-1. After deposition, the films are transferred to a furnace where they are annealed in flowing O_2 at 850°C for 2 h. The furnace then is turned off and allowed to cool to 100°C in about 16 h. Auger profiling of the films made by this process shows that the concentrations of Y, Ba, Cu, and O are uniform to within 1% throughout the thickness of the film.

TABLE 5-1		
Thin Film Parameters		
	Film 1	Film 2
Number of Layers	24	24
Thickness of Cu Layers	247 Å	246 Å
Ba Layers	840 Å	730 Å
Y Layers	201 Å	185 Å
Auger Composition	$\text{Ba}_1\text{Y}_{1.79}\text{Cu}_3$	$\text{Ba}_{0.9}\text{Y}_{1.53}\text{Cu}_3$
X-Ray Diffractometer	Polycrystalline, No Preferred Orientation	Polycrystalline, No Preferred Orientation
$T_c(R = 0)$	72 K	63 K

A cross section of the stripline resonator is shown in Figure 5-1. The structure is formed by three substrates. The top and central substrates are (1120) sapphire with a 4000-Å film of Nb deposited on them. The Nb on the central substrate has been patterned as a meander line as indicated in Figure 5-2. The lower YSZ substrate supports the films of YBaCuO that are being evaluated.

The gaps at the ends of the meander line provide capacitive coupling to the central section of the line. The structure resonates at frequencies for which the length of the line corresponds to integral multiples of half of the wavelength. The Q at each resonant frequency is evaluated by measuring the frequency response of the resonator using a network analyzer.

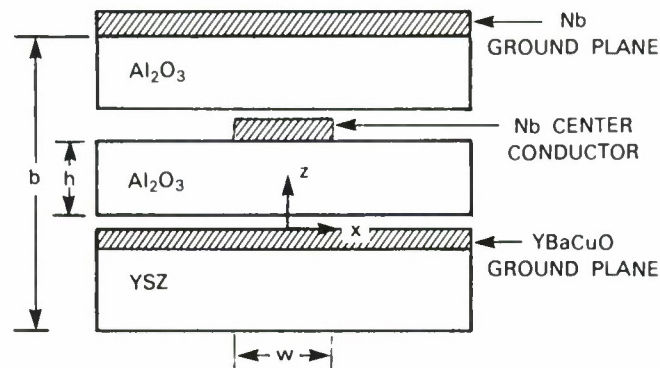


Figure 5-1. Cross section of the stripline resonator.

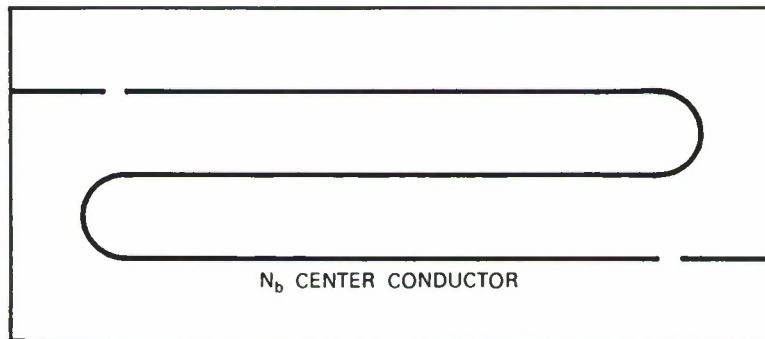


Figure 5-2. Meander-line pattern used for the center conductor of the resonator.

92044-19

92044-20

The quality factor Q can be expressed as

$$Q^{-1} = Q_C^{-1} + Q_D^{-1} + Q_L^{-1} \quad (5-1)$$

where Q_C is associated with losses in the conductors, Q_D with losses in the dielectric, and Q_L with the loading of the resonator by the external measurement circuit. The gaps in the center conductor are chosen to give a sufficiently weak coupling of the resonator to the external circuit that the Q_L term can be ignored. Also, the dielectric losses in our sapphire substrates are known to be much smaller than the losses associated with the Nb conductor over the frequency range $0.5 < f < 17$ GHz, so that $Q_D \gg Q_C$. Thus, the losses are almost entirely due to the conductors, and we may write $Q = Q_C$.

The surface resistance of the YBaCuO ground plane can be obtained from the measured Q by noting that for a transmission line resonator⁵

$$Q = \pi f / \alpha_c v_p \quad (5-2)$$

where α_c is the amplitude attenuation constant for the line, v_p is the phase velocity, and f is the resonant frequency. Since the stripline geometry used is essentially a TEM structure, $v_p = c / \epsilon_r^{1/2}$ where ϵ_r is the effective relative dielectric constant of the substrate.

Relating α_c of a superconductive stripline to the surface resistance of the superconductors requires a detailed knowledge of the distribution of currents in the central conductor and in the ground planes. We proceed by observing that, in all our measurements, the quality factors measured for the resonators containing a YBaCuO ground plane were significantly smaller than those obtained with an all-Nb stripline. We can then consider all the losses associated with the measured Q as being due to the YBaCuO ground plane. The surface resistance R_s is related to α_c by⁶

$$\alpha_c = \frac{1}{2Z_0} \int_{-\infty}^{+\infty} R_s \frac{[J_g(x)]^2}{I^2} dx \quad (5-3)$$

where the integral reflects the power loss in the ground plane per unit length in the direction of the power transmission. Here, Z_0 is the characteristic impedance of the line, $J_g(x)$ is the current distribution in the ground plane, and I is the total current. The geometry is as shown in Figure 5-1.

The distribution $J_g(x)$ can be calculated numerically using an image method.⁷ Alternatively, Equation (5-3) can be evaluated simply using an incremental inductance method first suggested by Wheeler.⁸ A detailed account of these calculations will be presented elsewhere. For our case, with $w = 150 \mu\text{m}$, $h = 880 \mu\text{m}$, a conductor thickness of $0.3 \mu\text{m}$, and $\epsilon_r = 10.1$, we obtain using either method

$$\alpha_c = 1.93 R_s (\Omega) \text{ m}^{-1} \quad (5-4)$$

The surface resistance R_s of the YBaCuO ground plane may be related to the measured Q of the resonator by combining (5-4) and (5-2):

$$R_s = 17.3 f(\text{GHz}) / Q \text{ ohms} \quad (5-5)$$

Note that (5-5) is generally applicable to any material used for the bottom ground plane provided that the losses in the material are much greater than the losses in Nb.

To check the stripline measurement method, we evaluated the surface resistance of a pure gold film and of an aluminum film that have resistivity ratios $R(T = 300 \text{ K})/R(T = 4.2 \text{ K})$ larger than 100. In this case, the surface resistance is limited at liquid helium temperatures by the anomalous skin effect. In Figure 5-3, we have indicated the experimental results for the YBaCuO films as well as the measured values for Al and Au films. The theoretical curves were obtained from the application of the Pippard formula.³ As we see from the graph, the experimental results for both Au and Al fall within experimental error of the calculations, indicating the validity of our measurement method.

In order to evaluate the losses of the YBaCuO up to its transition temperature, a stripline resonator has to be made in which all the conductors are YBaCuO. The dielectric losses of the YSZ then have to be evaluated to assure that they do not dominate the conductor losses. We have used the same stripline method with Nb conductors deposited on YSZ to evaluate the loss tangent of YSZ at 4.2 K.

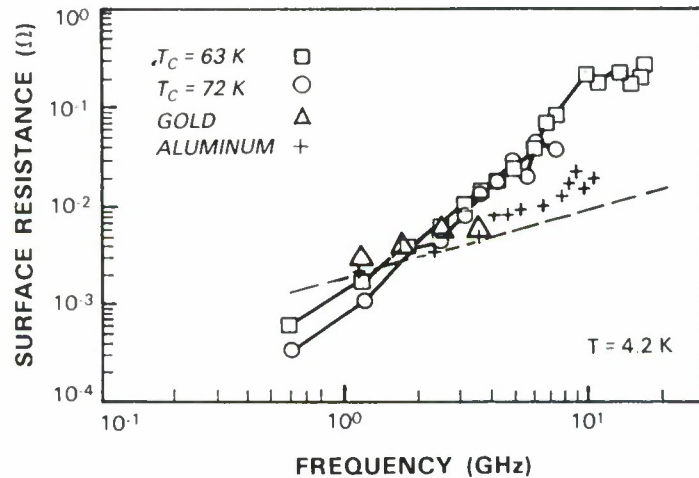


Figure 5-3. Surface resistance of YBaCuO, Au, and Al films as a function of frequency at 4.2 K.

The losses measured in this resonator were two orders of magnitude higher than for an equivalent structure built on sapphire, indicating that dielectric losses in the substrate dominate. Further indication of this is that, except for some scatter of the data at lower frequencies, the Q of the resonator is almost frequency independent. For a resonator dominated by dielectric losses, $Q^{-1} = \tan \delta = \epsilon''/\epsilon'$, where ϵ' and ϵ'' are the real and imaginary components of the dielectric constant of YSZ, respectively. The frequency independence of Q indicates that $\tan \delta$ is also constant, which is common for many dielectrics. The results for the dielectric losses are shown in

Figure 5-4. The real part of the dielectric constant determined from the values of the resonant frequencies was 25 and was constant in the frequency range $0.5 < f < 17$ GHz.

A.C. Anderson B-Y. Tsaur
J.W. Steinbeck M.S. DiIorio

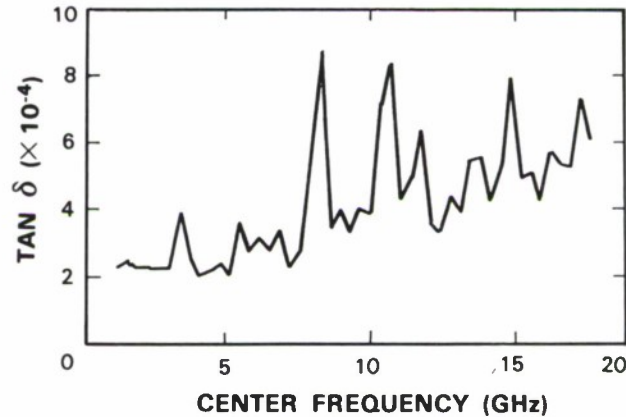


Figure 5-4. Measured values of the dielectric loss tangent of yttria-stabilized zirconia substrates at $T = 4.2$ K.

5.2 LASER DIRECT WRITE COMPENSATION OF REFLECTIVE-ARRAY COMPRESSOR

A suitable process for laser direct write compensation of reflective-array compressors (RACs) has been provided. A simple, stable, and environmentally insensitive amplitude-compensation process has been developed⁹ and used. The Mo photochemical etching process developed earlier¹⁰ has been retained for phase compensation.

The continuous weak reflection model of the RAC as modified to account for spatial amplitude and phase distortions has been demonstrated¹¹ to predict quantitatively our experimental spatial distortion results to within 10% and thereby to provide a basis for a compensation algorithm in which device errors can be expected to be reduced by an order of magnitude.

Direct trimming of amplitude and phase response of an RAC was demonstrated on a device with a time-bandwidth product of 130 and a center frequency of 106 MHz. To this end, a featureless cermet strip approximately 1.6 mm wide was sputter-deposited in the 2.7-mm space between the RAC gratings during initial device fabrication. Subsequently, a 1.0-mm Mo strip was e-beam evaporated alongside the cermet on the LiNbO_3 surface. The device was mounted in its final vacuum-tight package and photochemically processed.

Accurate spatial-domain correction patterns for high-resolution trimming were obtained by suitably deconvolving the effects of the grating kernel function from temperature-stable frequency-domain measurements. A single compensation without iteration was applied. A second compensation is expected to improve this final response.

The uncompensated frequency response with an initial 0.4-dB tilt across the design bandwidth was corrected to be uniform to within ± 0.05 dB as shown in Figure 5-5. The small residual bow in the response across the band may be attributed to a small nonuniform attenuation characteristic of the cermet film across the length of the RAC. The Fresnel ripple at the band edges is expected. In an ideal device with squared-off grating ends, the Fresnel response is symmetric with a 0.75-dB peak response.

As shown in Figure 5-6, full compensation of the device reduced the rms phase error from 1.5° to 0.5° . The origin of a residual 0.3° peak cubic harmonic component is unexplained.

In terms of a pulse-compression system, these measured device characteristics would support a weighting function with a 52-dB sidelobe level. This compares to a sidelobe level of approximately 39 dB in the best of devices as conventionally fabricated and compensated.

Application of these compensation techniques has resulted in significantly improved RAC response characteristics. Added improvement can be expected with refinement of these techniques.

V.S. Dolat
D.J. Ehrlich
J.H.C. Sedlacek

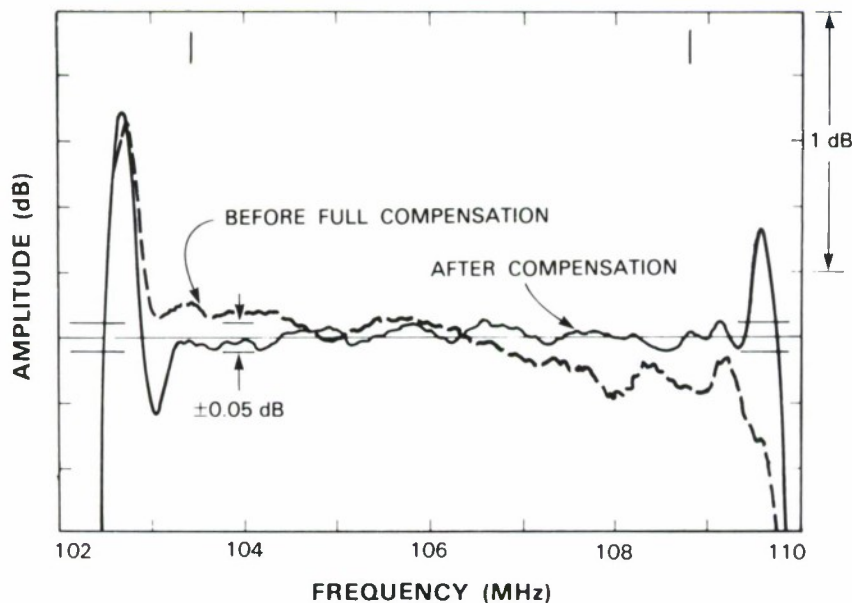


Figure 5-5. RAC frequency response before and after full compensation. Vertical lines near upper frequency axis indicate the design bandwidth of this device.

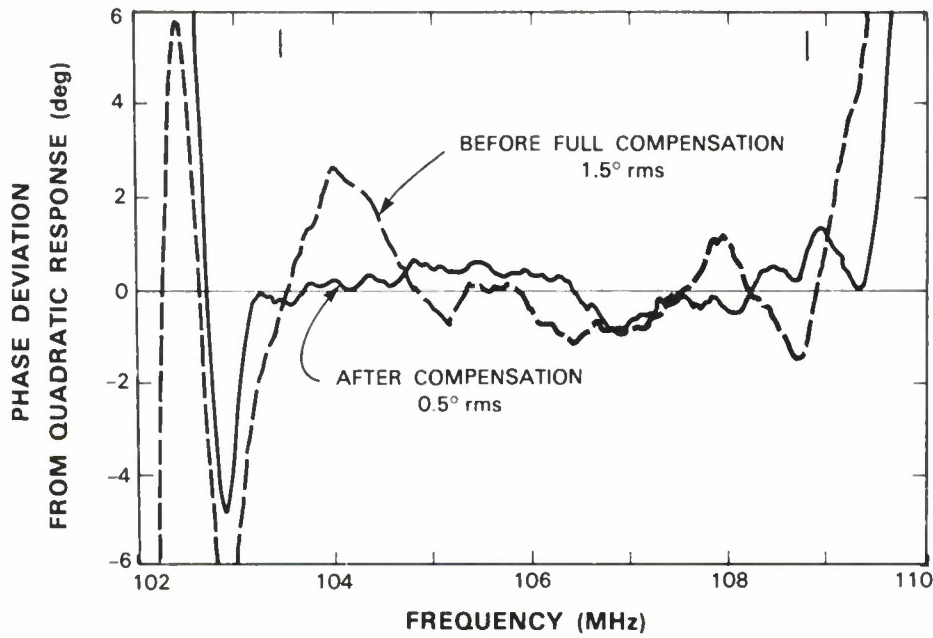


Figure 5-6. Corresponding RAC phase errors. A single phase-compensation pattern was applied after amplitude correction.

5.3 BULK-ACOUSTIC-WAVE REFLECTION-GRATING RESONATORS: PHASE-NOISE MEASUREMENTS AND TEMPERATURE COMPENSATION

Phase-noise measurements were made using the LiNbO_3 bulk-acoustic-wave (BAW) resonators fabricated as described previously¹² except that the acoustic transducer was a deposited thin film of ZnO. Several pairs of resonators were measured, all with resonant frequencies between 1.0 GHz and 1.25 GHz. Figure 5-7 shows the results of phase-noise measurement with two oscillators operating at 1.019 GHz. This represents our best phase-noise performance obtained to date, and the results in all cases are consistent with the parameters of the resonators and circuits.

The solid line shows the results obtained for the single-sideband phase noise using the standard model of a feedback oscillator.¹³ From this model, the single-sideband noise power in a 1-Hz bandwidth relative to the carrier power is given by

$$L(\omega) = 10 \log \left[N^2 \left(1 + \frac{\omega_0^2}{4Q^2\omega^2} \right) \left(\frac{GFkT}{P_c} + \frac{\alpha}{\omega} \right) \right] \quad (5-6)$$

where $L(\omega)$ is in dBc/Hz, P_c is the oscillator power, G the loop gain, F the amplifier noise figure, ω the offset frequency, Q the resonator quality factor, ω_0 the oscillator fundamental frequency, α the flicker-noise constant which must be empirically determined, and N the frequency-multiplication factor.

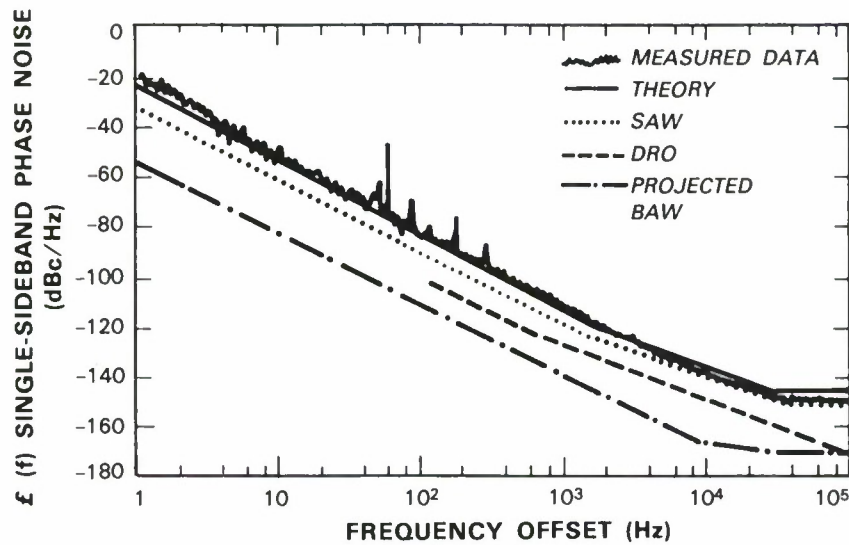


Figure 5-7. Results of measurements of phase noise in BAW-resonator-stabilized oscillators. For reference, the noise in a typical SAW oscillator multiplied up to 1-GHz operation and noise for a DRO at 1 GHz are shown. Also shown is a theoretical curve obtained using Equation (5-6) with $G = 40$ dB, $F = 3$ dB, $P_c = 16$ dBm, $Q = 2.0 \times 10^4$, and $\alpha = 1.6 \times 10^{-11}$. The agreement between theory and experiment is excellent. The bottom curve shows the projected noise with improvements discussed in text, using Equation (5-6) with $G = 25$ dB, $F = 4$ dB, $P_c = 27$ dBm, $Q = 5 \times 10^4$, and $\alpha = 2 \times 10^{-12}$.

To obtain the curve given in Figure 5-7, the following parameters were used: $G = 40$ dB, $F = 3$ dB, $P_c = 16$ dBm, $Q = 2 \times 10^4$ and $\alpha = 1.6 \times 10^{-11}$. The value of α was determined by measuring the $1/f$ noise of the amplifiers in the circuit. It is significant that the entire $1/f^3$ contribution comes from the $1/f$ noise of the amplifiers and that the resonators themselves seem to be free of added contributions. This is in contrast to the case of surface-acoustic-wave (SAW) resonators where the resonator itself contributes to the $1/f^3$ part of the phase-noise curve because of significant $1/f$ noise generated in the resonator.¹⁴ As can be seen from the figure, the agreement between model and experiment is quite good over the most of the range of measurement.

Figure 5-7 also compares these results with other technologies that have been described in the literature. The SAW results are for a typical resonator operating at 500 MHz and doubled to 1 GHz. The dielectric-resonator oscillator (DRO) data is from Reference 15. Also shown in Figure 5-7 are the results given by Equation (5-6) for a set of projected parameters for the BAW resonators. We conservatively project that we can run with a loop gain of 25 dB; this includes an insertion loss of 15 dB for the device, 3 dB for the filter, 3 dB for the phase shifter, and allows for some margin. The noise figure F is 4 dB. We estimate a P_c of +27 dBm; since we already have run an oscillator at +22 dBm, the extension to +27 dBm seems straightforward. We furthermore project a Q of 5×10^4 . This is still less than the material limit at 1 GHz and should be obtainable with improvements in the optical system. The projection also assumes a value of α equal to 2×10^{-12} , which we feel is easily achievable since even lower values have been reported.¹⁴

The temperature coefficient of delay (frequency) of Z-propagating compressional waves in LiNbO_3 has been measured to be $40 \text{ ppm } ^\circ\text{C}^{-1}$. While for some applications this temperature dependence of the resonant frequency is not a problem, in general, a temperature-stabilized oven will be required for the Fe:LiNbO_3 resonators. In order to operate a BAW holographic resonator without an oven, we have investigated the possibility of finding a material with a temperature-compensated cut and propagation mode. As far as we are aware, LiNbO_3 has no temperature-compensated direction for bulk acoustic waves.

Lithium tantalate, however, has been shown to have temperature-stable BAW cuts¹⁶ and has been shown as well to be a photorefractive material that can support optical holograms.¹⁷ LiTaO_3 is also well known as a high-acoustic-Q material and in the Z-propagation direction has been reported to have lower loss than LiNbO_3 .¹⁶ In this regard, we have investigated fabrication of holographic resonators in Fe:LiTaO_3 . Figure 5-8 shows the reflection coefficient for a sample of Fe:LiTaO_3 into which a hologram was written in the same manner as described previously for Fe:LiNbO_3 . This result is for a compressional wave propagating in the Z-direction and for the hologram k-vector also in the Z-direction. Clearly the Fe:LiTaO_3 functions in a way comparable to Fe:LiNbO_3 for a compressional wave propagating in the Z-direction.

Calculations were undertaken to locate a cut of LiTaO_3 with zero temperature coefficient of delay. Because the internal fields in the material are such that the Z-direction is the one with the most easily written holograms, we investigated cuts close to the Z-axis. A cut was identified and Figure 5-9 shows results of measurements of the fractional change in delay for a shear wave with direction cosines of 0.26, 0.34, and 0.90. Further measurements are currently under way to find a turnover temperature closer to room temperature.

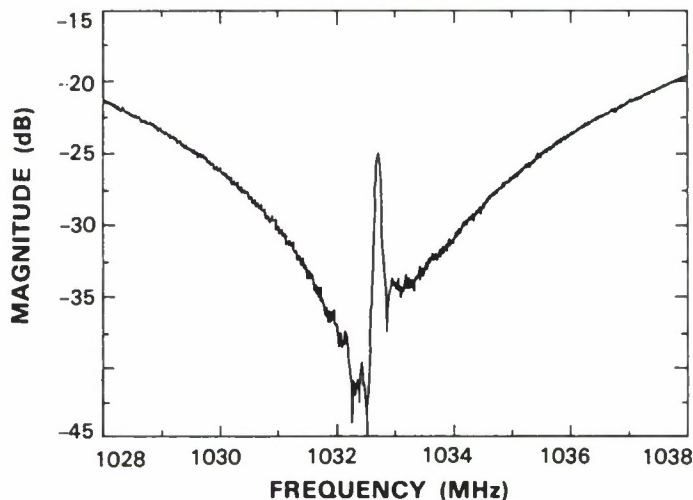


Figure 5-8 Reflection coefficient for a resonator fabricated in LiTaO_3 .

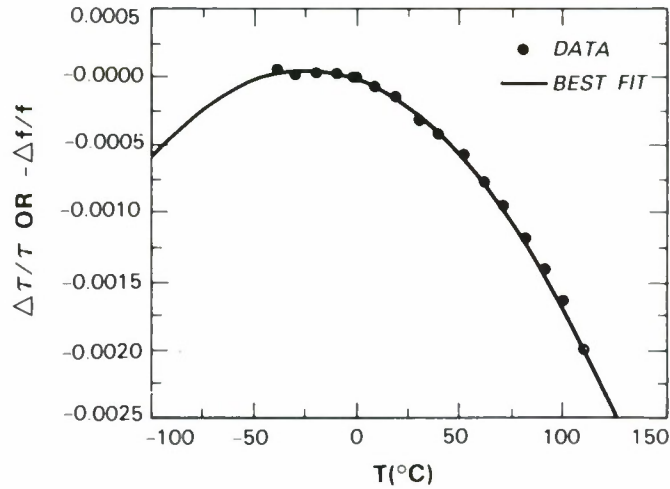


Figure 5-9. Measurements of relative change in delay vs temperature for new cut of LiTaO₃ employing shear wave propagation.

The temperature-compensated mode, however, is a shear wave. Although our LiNbO₃ work has been predominantly with compressional BAW, we have verified that a resonator can be fabricated using a shear wave. We anticipate, therefore, that temperature-stable shear-mode resonators can be developed in Fe:LiTaO₃. However, the use of shear waves may preclude the use of ZnO thin-film transducers and require instead bonded platelet technology.

We have demonstrated good performance in BAW reflection-grating resonators and demonstrated continuing improvements leading to the goal of very low phase noise using an inexpensive and readily manufacturable technology operating at fundamental frequencies of 1 GHz and above. We also have demonstrated, in principle, that temperature-compensated resonators can be fabricated in LiTaO₃. Efforts are under way to achieve the goal of temperature compensation and to investigate the possible Q factors and insertion loss as well as measurements of the phase noise.

D.E. Oates
J.Y. Pan

REFERENCES

1. J.G. Bednorz and R.A. Muller, *Z. Phys. B* **64**, 189 (1986).
2. A.P. Malozemoff, W.J. Gallagher, and R.E. Schwall in *Chemistry of High-Temperature Superconductors*, edited by D.L. Nelson, M.S. Wittingham, and T.F. George (ACS Symposium Ser. No. 351, 1987).
3. A.B. Pippard, *Advances in Electronics and Electron Phys.* **6**, 1 (1954).
4. B-Y. Tsaur, M.S. DiIorio, and A.J. Strauss, *Appl. Phys. Lett.* **51**, 858 (1987).
5. G.L. Matthaei, L. Young, and E.M.T. Jones, *Microwave Filters, Impedance-Matching Networks and Coupling Structures* (McGraw-Hill, New York, 1964), p. 217.
6. R.A. Pucel, D.J. Masse, and C.P. Hartwig, *IEEE Trans. Microwave Theory Tech.* **MTT-16**, 342 (1968).
7. T. VanDuzer and C.W. Turner, *Principles of Superconductive Devices and Circuits* (Elsevier, New York, 1981), p. 112.
8. H.A. Wheeler, *Proc. IRE* **30**, 412 (1942).
9. Solid State Research, Lincoln Laboratory, MIT (1987:1), p. 60, DTIC AD-A185987.
10. Solid State Research, Lincoln Laboratory, MIT (1985:1), p. 51, DTIC AD-A160922.
11. Solid State Research, Lincoln Laboratory, MIT (1986:4), p. 58, DTIC AD-A182215.
12. Solid State Research, Lincoln Laboratory, MIT (1987:1), p. 63, DTIC AD-A185987.
13. T.E. Parker, "Surface-Acoustic-Wave Oscillators," in *Precision Frequency Control Vol. 2*, edited by E.A. Gerber and A. Ballato (Academic Press, Orlando, Florida, 1985), p. 66.
14. T.E. Parker, in *Proceedings of the 41st Annual Symposium of Frequency Control — 1987* (to be published).
15. G.D. Alley and H.C. Wang, *IEEE Trans. Microwave Theory Tech.* **MTT-17**, 969 (1979).
16. S.V. Krishnaswamy, B.R. McAvoy, H.L. Salvo, and R.A. Moore, in *1984 Ultrasonics Symposium Proceedings* (IEEE, New York, 1984), p. 421.
17. E. Kraetzig and R. Orlowski, *Appl. Phys.* **15**, 133 (1978).

REPORT DOCUMENTATION PAGE

1a. REPORT SECURITY CLASSIFICATION Unclassified			1b. RESTRICTIVE MARKINGS			
2a. SECURITY CLASSIFICATION AUTHORITY			3. DISTRIBUTION/AVAILABILITY OF REPORT Approved for public release; distribution unlimited.			
2b. DECLASSIFICATION/DOWNGRADING SCHEDULE						
4. PERFORMING ORGANIZATION REPORT NUMBER(S) 1987:4			5. MONITORING ORGANIZATION REPORT NUMBER(S) ESD-TR-87-251			
6a. NAME OF PERFORMING ORGANIZATION Lincoln Laboratory, MIT		6b. OFFICE SYMBOL (If applicable)		7a. NAME OF MONITORING ORGANIZATION Electronic Systems Division		
6c. ADDRESS (City, State, and Zip Code) P.O. Box 73 Lexington, MA 02173-0073			7b. ADDRESS (City, State, and Zip Code) Hanscom AFB, MA 01731			
8a. NAME OF FUNDING/SPONSORING ORGANIZATION Air Force Systems Command, USAF		8b. OFFICE SYMBOL (If applicable)		9. PROCUREMENT INSTRUMENT IDENTIFICATION NUMBER F19628-85-C-0002		
8c. ADDRESS (City, State, and Zip Code) Andrews AFB Washington, DC 20334			10. SOURCE OF FUNDING NUMBERS			
			PROGRAM ELEMENT NO. 63250F	PROJECT NO. 649L	TASK NO.	WORK UNIT ACCESSION NO.
11. TITLE (Include Security Classification) Solid State Research						
12. PERSONAL AUTHOR(S) Alan L. McWhorter						
13a. TYPE OF REPORT Quarterly Technical Report		13b. TIME COVERED FROM <u>1 Aug</u> TO <u>31 Oct 87</u>		14. DATE OF REPORT (Year, Month, Day) 15 November 1987		15. PAGE COUNT 84
16. SUPPLEMENTARY NOTATION None						
17. COSATI CODES			18. SUBJECT TERMS (Continue on reverse if necessary and identify by block number)			
FIELD	GROUP	SUB-GROUP	solid state devices lasers microwave semiconductor devices quantum electronics laser arrays dry etching materials research wavefront sensor switched capacitors microelectronics infrared detectors superconductors analog device technology backgating acoustic-wave devices			
19. ABSTRACT (Continue on reverse if necessary and identify by block number)						
<p>This report covers in detail the solid state research work of the Solid State Division at Lincoln Laboratory for the period 1 August through 31 October 1987. The topics covered are Solid State Device Research, Quantum Electronics, Materials Research, Microelectronics, and Analog Device Technology. Funding is provided primarily by the Air Force, with additional support provided by the Army, DARPA, Navy, SDIO, NASA, and DOE.</p>						
20. DISTRIBUTION/AVAILABILITY OF ABSTRACT <input type="checkbox"/> UNCLASSIFIED/UNLIMITED <input checked="" type="checkbox"/> SAME AS RPT. <input type="checkbox"/> DTIC USERS				21. ABSTRACT SECURITY CLASSIFICATION Unclassified		
22a. NAME OF RESPONSIBLE INDIVIDUAL Lt. Col. Hugh L. Southall, USAF				22b. TELEPHONE (Include Area Code) (617) 981-2330		22c. OFFICE SYMBOL ESD/TML